Exploring Bipolar Membranes for Electrochemical Carbon Capture

Justin C. Bui[1,2], Éowyn Lucas[3,4], Eric W. Lees[2], Andrew K. Liu[1,2], Harry A. Atwater[3,4], Chengxiang Xiang[3], Alexis T. Bell[1,2], & Adam Z. Weber[2*]

[1] Department of Chemical and Biomolecular Engineering
University of California Berkeley
Berkeley, CA 94720, USA

[2] Liquid Sunlight Alliance
Lawrence Berkeley National Laboratory
Berkeley, CA 94720, USA

[3] Liquid Sunlight Alliance
California Institute of Technology
Pasadena, CA 91125, USA

[4] Department of Applied Physics
California Institute of Technology
Pasadena, CA 91125, USA

Corresponding Author: azweber@lbl.gov
Phone: (510) 486-6308

Abstract

Carbon dioxide (CO_2) must be removed from the atmosphere to mitigate the negative effects of climate change. However, the most scalable methods for removing CO_2 from the air require heat from fossil-fuel combustion to produce pure CO_2 and continuously regenerate the sorbent. Bipolar-membrane electrodialysis (BPM-ED) is a promising technology that uses renewable electricity to dissociate water into acid and base to regenerate bicarbonate-based CO_2 capture solutions, such as those used in chemical loops of direct-air-capture (DAC) processes, and also in direct-ocean capture (DOC) to promote atmospheric CO_2 drawdown via decarbonization of the shallow ocean. However, a lack of understanding of the mechanisms of reactive carbon species transport in BPMs has precluded industrial-scale deployment of BPM-ED. In this study, we develop an experimentally-validated 1D model for the electrochemical regeneration of CO_2 from bicarbonate-based carbon capture solutions and seawater using BPM-ED. Our experimental and computational results demonstrate that out-of-equilibrium buffer reactions within the BPM drive the formation of CO_2 at the BPM/electrolyte interface with energy-intensities of less than 150 kJ mol^{-1}. However, high rates of bubble formation increase the energy intensity of CO_2 recovery at current densities >100 mA cm^{-2}. Sensitivity analyses show that optimizing the BPM and bubble removal could enable CO_2 recovery from bicarbonate solutions at energy intensities <100 kJ mol^{-1} and current densities >100 mA cm^{-2}. These results provide design principles for industrial-scale CO_2 recovery using BPM-ED.

Broadness and Impact

Bipolar-membrane electrodialysis (BPM-ED) carbon capture uses renewable electricity to drive the capture and release of carbon dioxide (CO_2), making it a potentially important tool in the fight against climate change. This process employs BPMs to generate pH-swings for CO_2 capture and has been demonstrated at the lab scale at current densities exceeding 100 mA cm^{-2}. However, the energy required to drive BPM-ED (>300 kJ mol^{-1}) is prohibitive for industrial deployment. This study optimizes BPM-ED using a continuum modeling approach validated by experiment, which quantifies the energy intensity of BPM-ED and resolves the transport and dynamic equilibrium of reactive carbon species in BPMs. Applied-voltage-breakdown analysis identifies the dominant energy losses and elucidates BPM properties that improve the efficiency of BPM-ED. The model reveals that mitigation of generated CO_2 bubbles and acceleration of water-dissociation catalysis could reduce the energy intensity to <80 kJ mol^{-1} at 100 mA cm^{-2}, demonstrating potential for achieving high rates with substantially reduced energy penalties. This study provides insights into the physics of BPMs immersed in reactive carbon solutions and contributes towards the development of BPMs for electrochemical CO_2 reduction, cement production, and other emerging electrochemically decarbonized applications.

1. Introduction

Carbon-dioxide (CO_2) emissions account for 76% of total greenhouse-gas emissions and are currently 50% higher than pre-industrial levels. As a result, temperatures are expected to rise at least 2°C unless CO_2 is captured and removed from the atmosphere.[1–3] Traditional direct-air-capture technologies (DAC),[4] use alkaline aqueous sorbents (*e.g.*, $KOH_{(aq)}$) to capture ambient CO_2 as mixtures of (bi)carbonates, which are thermally-decomposed into a pure CO_2 gas stream for permanent removal (**Figure 1a**). Unfortunately, this technology is energy intensive and expensive, largely because of the significant thermal energy penalty (>150 kJ mol^{-1}) required to regenerate the sorbent after it has captured CO_2 **(Figure 1a, Step 4)**.[5] This thermal energy is often provided by burning natural gas, which results in CO_2 emissions that reduce the net amount of CO_2 removed from the atmosphere by DAC.

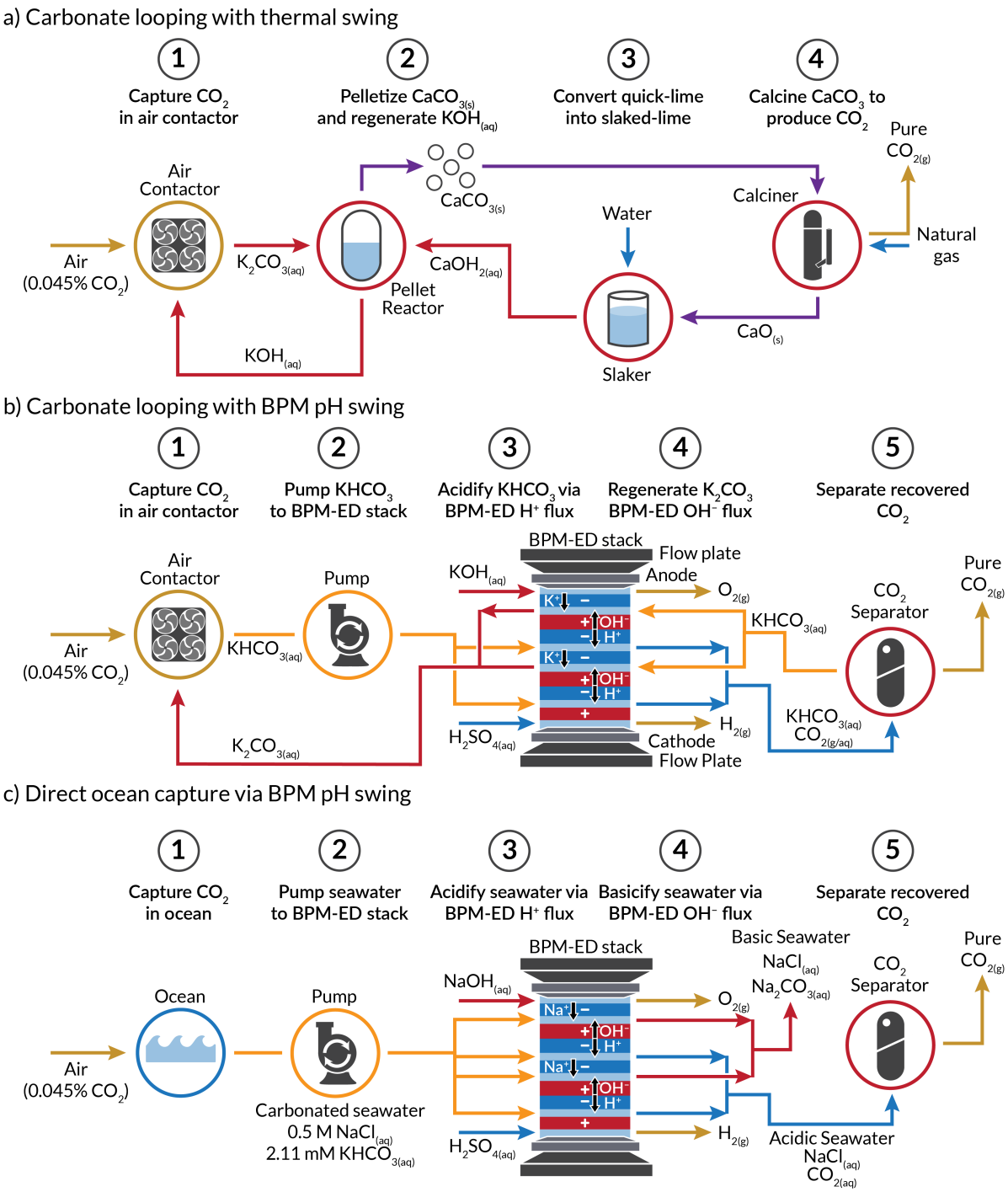

Figure 1: Process flow diagrams of various carbon capture processes. **(a)** Carbonate looping with thermal swing desorption. **(b)** Carbonate looping with electrochemical pH swing desorption via BPM. **(c)** Direct ocean capture with electrochemical pH swing desorption via BPM.

Electrochemically-mediated carbon capture (EMCC) can address the challenges associated with thermal sorbent regeneration by using low-cost renewable electricity to trigger the capture and release of CO_2 from the sorbent.[2,6–17] The low-temperature nature of EMCC also circumvents the thermal efficiency limits associated with desorbing CO_2 at high-temperature in fired reboilers and calciners.[18] Many chemistries have been explored for EMCC, such as nucleophilic sorbents that can absorb or desorb CO_2 when oxidized or reduced at an electrode surface[2,14,19,20] and amine-based sorbents that capture CO_2 homogeneously and release that CO_2 upon the reaction with cupric (Cu^{2+}) ions generated via electrochemical redox.[21,22] However, these specific EMCC technologies have not been demonstrated at current densities beyond 5 mA cm^{-2}, necessitating large, costly reactors or long residence times.[23,24]

Bipolar-membrane electrodialysis (BPM-ED) is a promising EMCC technology that uses water dissociation to mediate CO_2 capture and sorbent regeneration at relevant current densities (i.e., >100 mA cm^{-2}; **Figure 1b**).[16,17,25] At the heart of this technology is a BPM, which consists of anion- and cation-exchange layers (AEL and CEL) that are laminated together often with a catalyst layer (CL) at the interface. Under a reverse bias, the strong electric field formed at the interface of the oppositely-charged AEL and CEL layers drives water dissociation into acid (H^+) and base (OH^-) (Eq. (1)).[26,27] The acid produced in the CEL is used to shift the bicarbonate and carbonate equilibrium (Eq. (2)-(5)) towards CO_2,[26,28] and the base produced in the AEL is used to regenerate the alkalinity of the carbonate sorbent. A key advantage of BPM-ED is the use of water as the reactant, which enables higher current densities than other EMCC technologies because of the high concentration of water (55 M) in aqueous CO_2 capture solutions. Notwithstanding, the energy intensity of BPM-ED typically exceeds 300 kJ mol^{-1} because of the water dissociation

overpotential and ohmic resistances in the BPM. Further optimization is therefore required for BPM-ED to become more efficient than thermal CO_2 sorbent regeneration.[24]

BPM-ED is also capable of removing CO_2 from seawater at current densities exceeding 50 mA cm^{-2} (**Figure 1c**), *i.e.*, direct ocean capture (DOC).[7,297,16,17,25,30] By using seawater as the sorbent, instead of a concentrated bicarbonate solution, the natural process of CO_2 absorption and conversion into bicarbonates is leverged and obviates the need for a Capex-intensive air contactor.[4] In the DOC configuration, the OH^- transported from the AEL can be reacted with dissolved bicarbonates in the seawater to form a mineralized carbonate stream that can be precipitated and sequestered, or fed back into the ocean to help reverse the effects of ocean acidification.[31] CO_2 that is formed by BPM-ED can be collected outside the device for conversion or storage elsewhere,[7] or directly transported to a CO_2 reduction catalyst within the same device for direct conversion.[28,32]

The challenge with BPM-ED is that the energy intensities reported in the literature (300 to 1000 kJ mol^{-1} CO_2) are significantly higher than the minimum thermodynamic energy required to separate CO_2 from air (20 kJ mol^{-1}).[8] Unfortunately, while the mechanism of *in-situ* CO_2 capture and sorbent regeneration via BPM-ED has been well established experimentally,[32–34] very few theoretical studies have simulated BPMs immersed in carbon-containing solutions to resolve the dominant energy losses. Sabatino *et al.* developed process-level simulations to show the critical role BPM performance has on the energy intensity and overall technoeconomic feasibility of BPM-ED EMCC.[35,36] However, the simulations treated the BPM as a black-box, with no information

provided regarding ionic transport, water dissociation kinetics, or the material properties of the BPM that would be required to achieve the necessary performance enhancements.

Continuum models by Lees *et al.* and Kas *et al.* have helped to resolve the mechanism of *in-situ* CO_2 generation in BPM-based electrolyzers that convert (bi)carbonate capture solutions to carbon monoxide,[37,38] or methane.[28] However, these models only considered the CEL of the BPM, ignoring the AEL and the water dissociation CL where protons and hydroxide are generated. This simplification renders the models incapable of predicting the primary factors influencing the energy intensity of BPM-ED: carbon crossover, water dissociation overpotential, and ohmic loss.[39,40] There is also little precedent for modeling the transport of dilute carbon species in seawater feedstocks used for DOC.[7,41] Models that relate the chemistry and material properties of BPMs to the energy intensity of BPM-ED are therefore warranted.[42]

In this work, we demonstrate a comprehensive model of BPM-ED based on our prior work modeling multi-component transport in BPMs,[27] now with the homogeneous reaction kinetics of reactive carbon species (Eq. (2)-(5)). The model is validated by comparison with experimental data for various carbon-containing solutions, and is used to elucidate the nature of *in-situ* CO_2 generation and sorbent regeneration in BPMs employed for EMCC. Additionally, concentration profiles and fluxes of all carbon species, protons, and hydroxide anions are resolved such that performance tradeoffs between CO_2 generation and carbon crossover can be explored. Lastly, sensitivity analysis provides improved understanding of ideal BPM and system properties to enhance CO_2 capture efficiency, setting the stage for BPMs optimized for carbon capture processes.

2. Methods

2.1 Theory and Computational Methods

The BPM model employed here (described in detail in **Section S1** of the SI) was designed to mimic the 4-probe experiments performed for direct BPM analysis (described in detail in **Section S2.2**), modeling the relevant domain as a 1-dimensional (1D) continuum consisting of an 80 μm CEL, and an 80 μm AEL sandwiching a 3.5 nm water dissociation CL, with a 25 μm diffusion boundary layer (**Section S1.6**) on either side of the BPM assembly (**Figure 1**). Modeling the domain as such enables the capturing of all relevant concentration profiles and species fluxes. Importantly, the model also explicitly considers the generation and consumption of species *via* the homogeneous buffer reactions shown below. The effects of forced convection are implicitly considered as dictating the diffusion boundary-layer thickness, but convective effects are not explicitly considered within the modeled domain, because the electrolyte should be quiescent within the diffusion boundary layer.

$$H_2O \overset{k_1, k_{-1}}{\leftrightarrow} H^+ + OH^- \qquad K_1 = 1 \times 10^{-14} \qquad (1)$$

$$CO_{2(aq)} + H_2O_{(l)} \overset{k_2, k_{-2}}{\leftrightarrow} H^+_{(aq)} + HCO^-_{3(aq)} \qquad K_2 = 4.27 \times 10^{-7} \qquad (2)$$

$$HCO_3^- \overset{k_3, k_{-3}}{\leftrightarrow} H^+ + CO_3^{2-} \qquad K_3 = 4.58 \times 10^{-11} \qquad (3)$$

$$CO_{2(aq)} + OH^- \overset{k_4, k_{-4}}{\leftrightarrow} \leftrightarrow HCO_3^- \qquad K_4 = 4.27 \times 10^{7} \qquad (4)$$

$$HCO_3^- + OH^- \overset{k_5, k_{-5}}{\leftrightarrow} H_2O + CO_3^{2-} \qquad K_5 = 4.58 \times 10^{3} \qquad (5)$$

The simulated membrane potential across the 1D domain is equivalent to the measured membrane potential across the two reference electrodes in the 4-probe experiment. The choice of a 4-probe measurement (and simulation) is critical because it enables the decoupling of the potential losses that occur at the anode and cathode from those that result from and drive transport and kinetics in the BPM.[43] For the purposes of the simulations and energy intensity calculations, we defined the energy intensity of the BPM-ED processes as the membrane potential in the 4-probe experimental cell since the energetics of the terminal electrodes are not directly correlated with the rate of CO_2 efflux or sorbent regeneration in the BPM. Moreover, the terminal electrodes are often used to perform reactions that produce value-added streams in EMCC processes.[28,34] Terminal electrodes were considered in our BPM-ED stack analysis (**Section S24**) to compare the associated energy penalty to the overall cell voltage as the number of BPMs in the stack is increased.[30]

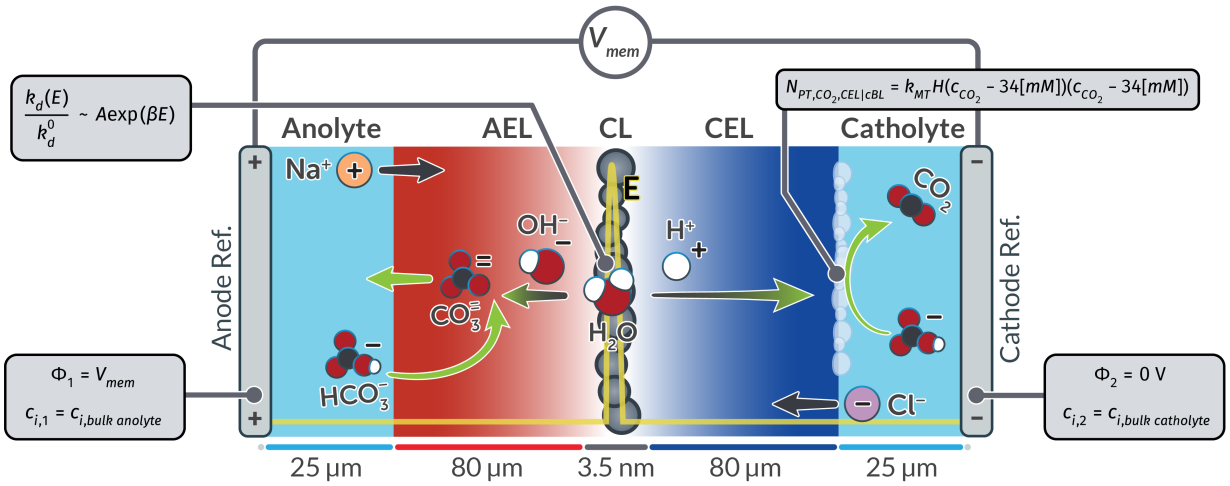

Figure 2: Schematic of simulated domain for BPM performing BPM-ED EMCC. H_2O at the interface of the AEL and CEL (in the CL) is reacted by electric-field-enhanced water dissociation to form H^+ and OH^-. The H^+ react with HCO_3^- in the catholyte to form CO_2. Once the *in situ* generated CO_2 has exceeded its solubility limit in the catholyte, it exits the aqueous phase in the form of bubbles. OH^- from water dissociation reacts with HCO_3^- absorbed in the AEL to form

CO_3^{2-} that transports back into the anolyte. Spectator co-ions from the anolyte or catholyte can cross through the membrane to reduce the developed pH gradient.

2.1.1 Thermodynamics of BPM-ED EMCC

To describe the thermodynamics of all species within the BPM, the following electrochemical potential expression is used[44,45]

$$\mu_i = \mu_i^0 + RT\ln(a_i) + z_i F\Phi\,, \tag{6}$$

where Φ is the electrostatic potential within the electrolyte and membrane phases and R, T, and F are the ideal gas constant, the temperature, and Faraday's constant, respectively. In the above expression, the first term is the reference chemical potential of species *i*, the second term accounts for changes in activity of *i*, the third term accounts for electrostatic potential and only applies for charged ionic species (*i.e.*, all species except CO_2). The activity (a_i) of a given species is defined by

$$a_i = \frac{f_i c_i c_{H_2O}^0}{c_{ref} c_{H_2O}}\,, \tag{7}$$

where c_{ref} is a reference concentration (1 M), and the ratio $\frac{c_{H_2O}}{c_{H_2O}^0=55.56[\mathrm{M}]} = \varepsilon_w$ is the water volume fraction and accounts for change in volumetric reference between the liquid electrolyte and liquid-filled channels of the BPM; in other words, equilibrium is calculated and upheld within the interstitial volume of the BPM. Note that ion specific partitioning was not considered in the model as the relevant parameters are currently unavailable. The activity coefficient (f_i) for charged species that participate in homogeneous buffer reactions (HCO_3^-, CO_3^{2-}, H^+, and OH^-) is a function of the electric field,

$$f_{i=OH^-,H^+CO_3^{2-},or\ HCO_3^-} = -|z_i|\sqrt{f(E)}, \tag{8}$$

where $|z_i|$ is the absolute value of the charge on species *i*, *E* is the local electric field, and $f(E)$ is the dependence of the macroscopic equilibrium constant on electric field, defined by the Second Wien Effect for net-charge-generating dissociation reactions (reactions 1, 2, and 3 above).[26,46–49]

$$f(E) = \frac{\left(\sum_{m=0}^{\infty}\frac{1}{m!(m+1)!}(2\beta E)^m\right)\cosh(\tau\beta E)\cosh(\tau)^{\beta E}}{1+\frac{1-\exp\left(-\frac{1}{\sigma}\right)}{2}\left(\sigma^2\beta E+(4.97\sigma)\frac{\sinh(0.0835\sigma\beta E)}{\cosh^2(0.0835\sigma\beta E)}\right)}. \tag{9}$$

where β, τ, and σ are lumped parameters discussed in more detail in **Section S1.3**. The dependence on *E* in equation (9) is approximately exponential, as shown in previous work.[26] The above dependence of the activity coefficient on the electric field ensures that macroscopic equilibrium is upheld (*e.g.*, $\mu_{H^+} + \mu_{OH^-} = \mu_{H_2O}$ for water dissociation or $\mu_{H^+} + \mu_{CO_3^{2-}} = \mu_{HCO_3^-}$ for bicarbonate dissociation) **(see Section S1.1** for consistency of macroscopic equilibrium), and results in the equilibrium constants of net-charge-generating reactions to be

$$K_{n=1,2,3}(E) = K_n(E=0)f(E) \tag{10}$$

where $K_{n=1,2,3}(E)$ is the equilibrium constant, which is a function of local electric field, and $K_n(E=0)$ is the value of the equilibrium constant for no applied electric field. For neutral species (*i.e.*, CO_2) and ions that do not participate in buffer reactions (*i.e.*, K^+), the activity coefficient is unaffected by the electric field. We note that ion-specific interactions likely impact ionic transport and concentrations in the BPM due to the high concentrations (> 1 M) in the BPM.[50,51] However, these are likely second-order effects and mixed-interaction parameters are not available for the broad variety of ions in the polymer membranes studied herein.

2.1.2 Kinetics of BPM-ED EMCC

Homogeneous reactions consume carbon-containing species, OH^-, and H_3O^+ throughout the electrolyte domain. The rate of consumption of species *i* in bulk reactions is given by the law of mass action:

$$R_{B,i} = \varepsilon_w \sum_n s_{i,n} \left(k_n \prod_{s_{i,n}<0} a_i^{-s_{i,n}} - k_{-n} \prod_{s_{i,n}>0} a_i^{s_{i,n}} \right) \tag{11}$$

Similar to how the macroscopic equilibrium is impacted by the electric field by the Second Wien Effect, the forward and reverse rate constants for net-charge-generating homogeneous reactions are affected by the electric field, with their electric-field-dependence taking the form of the numerator and denominator, respectively, of Equation (9).

$$\frac{k_n(E)}{k_n(E=0)} = \left(\sum_{m=0}^{\infty} \frac{1}{m!\,(m+1)!} (2\beta E)^m \right) \cosh(\tau\beta E) \cosh(\tau)^{\ \beta E} \tag{12}$$

$$\frac{k_{-n}(E)}{k_{-n}(E=0)} = 1 + \frac{1 - \exp\left(-\frac{1}{\sigma}\right)}{2} \left(\sigma^2 \beta E + (4.97\sigma) \frac{\sinh(0.0835\sigma\beta E)}{\cosh^2(0.0835\sigma\beta E)} \right) \tag{13}$$

To model the water dissociation catalyst, we treat the CL as a thin neutral region located between the AEL and CEL where the large field in between the two layers drives the dissociation of water by shifting the forward and reverse rate constants as per equations (12) and (13). While more detailed models of water dissociation catalysis have been presented that explicitly consider catalyst surface effects,[26,52] we choose a more simple model for water dissociation for computational efficiency. Furthermore, the interaction of carbon species with catalyst surfaces are still not well understood; because this work is more focused on modeling the impact of reactive carbon species on polarization behavior and mesoscale transport, the exact details of the

catalyst surface are not crucial to capture. More details on the choice of model for the CL can be found in **Section S1.4**.

2.1.3 Mass and Charge Conservation in BPM-ED EMCC

To solve for all concentrations and fluxes of relevant species (CO_2, OH^-, H^+, Cl^-, HCO_3^-, CO_3^{2-}, Na^+ and K^+), species conservation is used,

$$\nabla \cdot \boldsymbol{N}_i = R_{B,i}, \tag{14}$$

where $\boldsymbol{N}_i$ is the flux of species i, and $R_{B,i}$ is a source term defined as the generation of species i from homogeneous buffer reactions and water recombination/dissociation (described in detail in **Section 2.1.2**). The molar species flux is defined by the Nernst-Planck equation,

$$\boldsymbol{N}_i = -\frac{D_i c_i}{RT}\frac{d\mu_i}{dx}, \tag{15}$$

where D_i, c_i, μ_i are the diffusivity, concentration, and electrochemical potential of species i, respectively. Fluxes due to the second Wien effect modification to the Poisson Nernst Planck equations are also directly calculated from the derivative of the Wien Effect activity coefficient (equation (8)).

The Poisson equation is solved to determine the electrostatic potential,

$$-\frac{d^2\Phi}{dx^2} = \frac{F}{\varepsilon}\left(c_M(x) + \sum_i z_i c_i\right), \tag{16}$$

ε is the dielectric permittivity of the medium, defined to be that of water (ε_{H_2O}) in the electrolyte domains. For the membrane domains, the dielectric permittivity (ε_M) is defined by **Equation S36** in the SI.

The diffusivities, permittivities, and transport properties are calculated as per previous work.[53] The double-layer thickness is simulated by solution of the Wien-effect modified PNP and results from an assumed neutralization thickness of 3.5 nm at the AEL|CEL interface.[27,54] Discussion of the double layer simulation at the AEL|CEL interface can be found in prior work. Details on how the diffusivities and transport properties in the BPM are calculated can be found in **Section S1.5**.

2.1.4 Phase Transfer due to Bubbling and Bubble Coverage Effects

To account for the bubbling out of CO_2 gas at the catholyte/CEL interface, a phase transfer flux sink term is incorporated into the model that activates once the dissolved CO_2 concentration in the catholyte exceeds the saturation concentration (**Figure 2**),

$$N_{PT,CO_2,CEL|cBL} = k_{MT}\mathrm{H}\left(c_{CO_2,CEL|cBL} - 34\ [\mathrm{mM}]\right)\left(c_{CO_2,CEL|cBL} - 34\ [\mathrm{mM}]\right) \quad (17)$$

where k_{MT} is a mass transfer coefficient set to $1 \times 10^5\ \frac{\mathrm{m}}{\mathrm{s}}$ to ensure that any dissolved CO_2 beyond saturation immediately bubbles out of the electrolyte. $\mathrm{H}(x)$ is the Heaviside step function. $c_{CO_2,CEL|cBL}$ is the concentration of dissolved CO_2 in the catholyte side of the CEL|catholyte boundary-layer (cBL) interface.

Because the model immediately removes bubble CO_2 from the domain and does not track the bubble phase explicitly, to determine the gas bubble flux out of the domain, the model is run with and without the flux term shown in equation (17), and the flux of bubbles out of the domain ($j_{CO_2,bubble}$) is determined as the difference in CO_2 efflux between the simulations with and without implementation of equation (17) (**Figure S2**).

$$j_{bubble,CO_2} = j_{CO_2,out,no\ phase\ transfer} - j_{CO_2,out,with\ phase\ transfer} \quad (18)$$

In accordance with prior work examining the effect of gas bubbling on electrochemical systems,[55] the CO_2 bubbles, which are quite substantial (**see Supporting Video S1**), accumulate on the surface and reduce the electrochemically active surface area and consequently the current density that can be achieved. The bubble coverage ($\theta_{CO_2,bubble}$) is related to the bubble efflux and can be calculated by[55]

$$\theta_{CO_2,bubble} = 0.024\left(\frac{F\times j_{bubble,CO_2}}{1\ [mA\ cm^{-2}]}\right)^{0.55} \tag{19}$$

where the values of 0.024 and 0.55 in the above expression are fitted parameters that are consistent with prior implementations of the above model for bubble coverage.[55] The coverage term ($\theta_{CO_2,bubble}$) calculated using this semi-empirical model represents a site-blocking factor equal to the fraction of the areal cross section impeded by bubbles and thus inaccessible for ionic transport. Thus, once $\theta_{CO_2,bubble}$ is calculated, the simulated current density is corrected to account for the loss in active area due to bubble coverage:

$$i_{BPM} = i_{BPM,no\ bubble}\left(1-\theta_{CO_2,bubble}\right) \tag{20}$$

where $i_{BPM,no\ bubble}$ is the simulated BPM current density prior to post-processing with bubble coverage effects.

2.1.3 Boundary Conditions

Boundary conditions are shown in the schematic in **Figure 2**. At the end of anolyte boundary layer (leftmost boundary), Dirichlet boundary conditions set the concentrations of all modeled ionic species to their bulk electrolyte values,

$$c_i\big|_{x=-\frac{L_{CL}}{2}-L_{AEL}-L_{cBL}} = c_{i,anolyte}^{bulk} \tag{21}$$

where the origin (x = 0) is defined at the center of the CL, L_{CL} is the CL thickness, L_{AEL} is the AEL thickness, and L_{aBL} is the anolyte boundary-layer thickness. The thickness of both the catholyte and anolyte boundary layers are assumed to be equal to 25 μm, and are estimated by assuming approximately Fickian behavior of the CO_2 at the onset of bubbling (**Section S1.6**).

The electrostatic potential is set to the measured membrane potential with another Dirichlet boundary condition,

$$\Phi|_{x=-\frac{L_{CL}}{2}-L_{AEL}-L_{aBL}} = V_{mem} \tag{22}$$

At the end of the catholyte boundary layer (rightmost boundary), Dirichlet boundary conditions are again employed to set species concentrations to their bulk values (as defined by their equilibrium concentrations for the given (bi)carbonate salt concentration):

$$c_i|_{x=\frac{L_{CL}}{2}+L_{CEL}+L_{cBL}} = c_{i,catholyte}^{bulk} \tag{23}$$

L_{CEL} is the CEL thickness, and L_{cBL} is the anolyte boundary layer thickness. Lastly, the electrostatic potential is set to a reference of 0 V at the catholyte boundary,

$$\Phi|_{x=\frac{L_{CL}}{2}+L_{CEL}+L_{cBL}} = 0\ \text{V} \tag{24}$$

S2.1.4 Computational Methods

The governing equations representing this model were solved using two coupled General Partial Differential Equation (g) Modules in COMSOL Multiphysics 5.6. The modeling domain was discretized with a nonuniform mesh with heavy refinement near all interfaces (membrane-membrane, membrane-electrolyte, and membrane-CL) as well as within the CEL and catholyte where *in-situ* CO_2 generation occurs. The resulting mesh comprised 6000-18000 elements

depending on the applied current density. A mesh independence study was performed, and the results were found to be independent of meshing for those meshes. Critically, to achieve initial convergence, the Donnan equilibria were solved analytically to obtain species concentrations in each of the membrane layers at 0 applied membrane potential and fed to the simulation as initial conditions using hyperbolic tangent analytic functions. The simulations in the present study were solved using the Multifrontal Massively Parallel sparse direct Solver (MUMPS) using Newton's Method with a tolerance of 0.001 and a recovery damping factor of 0.75. For current densities where bubbling occurs, due to numerical instability, the tolerance was increased to 0.008 and the recovery damping factor reduced to 0.35.

2.2 Experimental Methods

2.2.1 Chemicals

All chemicals were used as purchased. Sodium hydroxide (NaOH, Macron Chemicals), sodium chloride (NaCl, VWR Chemicals), sodium bicarbonate ($NaHCO_3$, ≥99.5%, Sigma-Aldrich), potassium bicarbonate ($KHCO_3$, 99.7-100.5%, J. T. Baker), and potassium carbonate (K_2CO_3, 99.997%, Thermo Scientific). Simulated seawater in this work consists of 0.5 M NaCl with 0.00211 M $NaHCO_3$.

2.2.2 Electrodialysis Cell

Experimental current density-voltage measurements were obtained using a home-made five-chamber electrodialysis cell with Luggin capillaries. The cell was constructed, as depicted in **Figure S1,** using a Ni foil (VWR) anode and cathode, Nafion N324 CEMs (FuelCellStore), Fumasep FAB-PK-130 AEM (Fuelcellstore), and Fumasep FBM-PK BPM (FuelCellStore). The

active area of the BPM in this specific cell was 1 cm^2. Copper tape was used as leads for the Ni electrodes and Ag/AgCl (CH instruments, CHI111P) reference electrodes were placed in custom made glass Luggin capillaries on either side of the BPM.

2.2.3 Electrochemical measurements

Once the electrodialysis cell was assembled, a peristaltic pump (Ismatec ISM4408) was used to flow 1 M NaOH (10 mL min^{-1}) through the outer chambers, 3 M NaCl (10 mL min^{-1}) through the dilute chamber (chamber between CEM and AEM), and the relevant bicarbonate, carbonate, or simulated seawater solution (0.2 mL min^{-1}) through the chambers on either side of the BPM. These flowrates remained constant through all measurements. Once all chambers were filled, leads from a SP-300 BioLogic potentiostat were connected to the cathode, anode, and reference electrodes in a four-point measurement configuration. Current density-voltage measurements were then obtained by applying a chosen current across the cathode and anode and measuring the voltage between the two Ag/AgCl reference electrodes. Oxygen evolution was performed at the anode and hydrogen evolution was performed at the cathode. These reactions were isolated from the BPM with the two monopolar membranes positioned on either side. Measurements were started at 0.1 mA cm^{-2} and increased stepwise through each current density to 100 mA cm^{-2} (EC-lab® software). Each current step was held constant for 20 minutes to obtain a steady-state voltage. The final voltage collected at each current step was reported in the current density-voltage plots, with the exception of some of the higher current density steps. During the 1 M $KHCO_3$ and 0.5 M $KHCO_3$ experiments, CO_2 bubbles formed at the surface of the electrode at higher current

densities (≥ 20 mA cm^{-2}) causing a significant amount of noise in the data. For these measurements, the voltage reported was taken as the average over the current step.

3. Results and Discussion

3.1 Agreement with Experiment and Breakdown of Partial Current Density

To understand the transport and reaction kinetics of reactive carbon species in BPMs, experimental polarization curves were taken in a 4-probe experimental cell for a BPM immersed in three electrolytes relevant to EMCC and DOC applications: 1 M $KHCO_3$, 0.5 M $KHCO_3$, and simulated seawater (0.00211 M $NaHCO_3$ + 0.5 M NaCl). Simulations of the BPM under polarization in these varying electrolytes were run and the simulated polarization curves were compared to the experimentally measured polarization curves (**Figure 3a, markers**). Strong agreement between theory and experiments is observed in all three carbon-containing electrolytes for a single set of fitting parameters (**Table S4**). Remarkably, the simulation can even capture the incredibly non-intuitive polarization behavior occurring at current densities < 20 mA cm^{-2} (**Figure S3**). For these current densities, there is an initial onset in current density at ~0.4 V of applied membrane potential for both the 0.5 M $KHCO_3$ and 1 M $KHCO_3$ BPMs. The current density of these BPMs increases approximately linearly until ~0.7 V when the current density takes off exponentially. Conversely, for the seawater BPM, the current density does not have an initial takeoff at 0.4 V, so between 0.4 and 0.8 V the seawater BPM drives less current density than the $KHCO_3$ BPMs. However, past the second onset at ~0.7 V, the current generated in the seawater BPM exceeds that of the $KHCO_3$ BPMs. Notably, the initial linear takeoff of the $KHCO_3$ BPMs at 0.4 V of membrane potential, along with the intriguing intersection and crossover between the

seawater and (bi)carbonate polarization curves at ~0.75 V, represent heretofore unexplained phenomena that the model is capable of replicating with high accuracy.

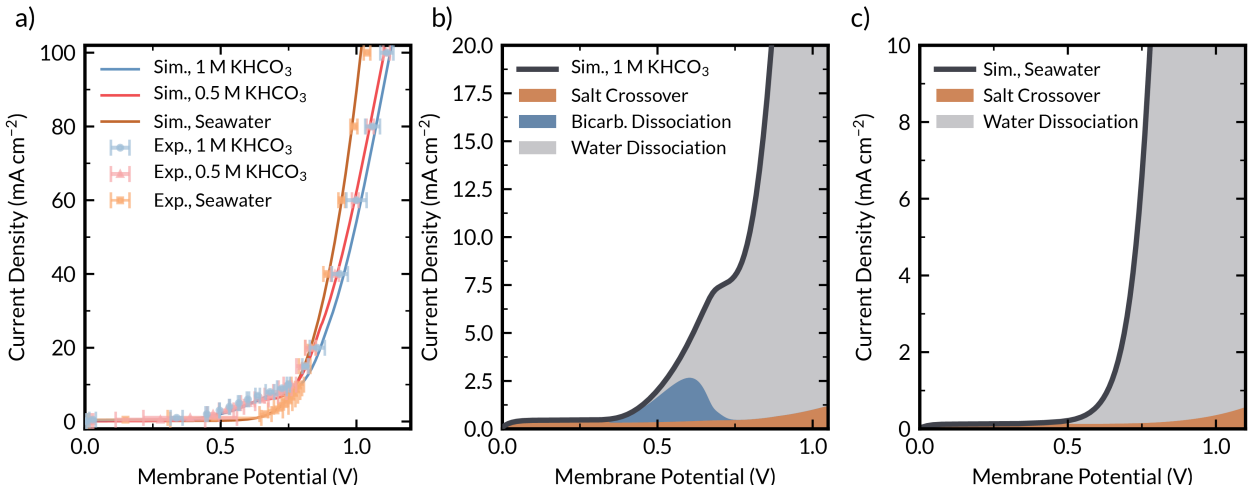

Figure 3: (a) Experimental (markers with error bars) and simulated (solid lines) polarization curves for BPMs immersed in various solutions of aqueous bicarbonate. **(b-c)** Breakdown of partial current density in the CL due to contributions of salt crossover (orange), bicarbonate dissociation (blue), and water dissociation (gray) for a BPM immersed in **(b)** 1 M $KHCO_3$ and **(c)** simulated seawater. The *y*-scale for panels **(b)** and **(c)** are zoomed into highlight the unique behavior of the carbon-containing BPMs at low current densities.

To uncover the origin behind these phenomena and deconvolute the individual contributions to the polarization curves of BPMs in reactive carbon solutions, the rates of the individual contributions to current density were calculated within the CL of the BPM. Within the CL, the current density must either be due to the crossover of unreactive co-ions (K^+, Na^+, or Cl^-), or to the presence of electric-field-enhanced, net-charge-generating dissociation reactions. These contributions to the overall polarization curve are determined and shown in **Figure 3b and 3c** for BPMs operating in 1 M $KHCO_3$ and simulated seawater, respectively. As expected, the current density for the simulated seawater case is primarily driven by salt crossover at low potentials and water dissociation at high potentials, as shown in previous literature.[27,56] The 1 M $KHCO_3$ case,

however, is more intriguing. While previous studies have suggested that the low applied potential current onset for BPMs in weak buffer electrolytes is entirely driven by titration currents resulting from dissociation of the weak acid buffer (*i.e.*, the HCO_3^- anion in this case) in the CL,[27,49,57] the model suggests that current density in the initial linear feature is still primarily dominated by field-enhanced water dissociation. Field-enhanced dissociation of the buffering anion accounts for up to 50% of the observed current density. Therefore, the model suggests that the use of 1 M $KHCO_3$ buffer electrolytes forces an early onset of the electric-field-enhanced water-dissociation reaction.

The simulations demonstrate that the accelerated current onset for $KHCO_3$-exchanged BPMs is largely due to a reduction in the rate of interfacial recombination due to reaction of water-dissociation-generated OH^- with HCO_3^- to form CO_3^{2-} *via* what is essentially an indirect HCO_3^- dissociation pathway (water dissociation followed by bicarbonate to carbonate interconversion), and that the eventual increase of the seawater current density beyond the $KHCO_3$ current densities is due to the seawater BPM possessing a larger electric field at a given membrane potential **(**see **Section S6** for more detail regarding the reasoning for the observed curvature of the BPM polarization curves in these carbon containing electrolytes).

3.2 Simulated Concentration Profiles of Ionic Species and CO_2

The validated model was employed to resolve local concentrations and microenvironments within BPMs exchanged with the aqueous reactive carbon solutions. The simulated concentration profiles of HCO_3^-, CO_3^{2-}, CO_2, and H^+ within a BPM exchanged with 1 M $KHCO_3$ at applied potentials of 0 V, 0.2 V, 0.5 V, and 1.0 V, are shown in **Figure 4**. Concentration profiles for OH^- as

well as local pH can be found in **Figure S14-15**. At equilibrium (0 V), both electrolyte boundary layers are fixed at their equilibrium concentrations for all species. Furthermore, within the BPM, there are no concentration gradients, and the concentrations are consistent with those determined by Donnan equilibrium with the interstitial pore volume.[27,56] Because of Donnan equilibrium with the catholyte, the CEL is fully exchanged with K^+ cations (**Figure S16-17**), and the AEL is fully exchanged with (bi)carbonates. Therefore, the pH in the CEL at equilibrium is near neutral, and that in the AEL is alkaline (~pH 9) (**Figure S14b**).

As the applied potential increases, the pH within the CEL decreases significantly due to the generation of H^+ via water dissociation and bicarbonate dissociation. Consistent with the equilibria presented in equations (1)-(5), as the pH in the CEL decreases, the concentrations of OH^-, CO_3^{2-}, and HCO_3^- decrease, and the concentration of CO_2 in the CEL increases. Additionally, diffusion gradients manifest in K^+ to maintain electroneutrality with the water-dissociation-generated H^+. Importantly, the model enables spatial resolution of *in-situ* CO_2 regeneration, which is shown to occur only at the CEL|cBL interface, because the concentration of (bi)carbonates are too small within the CEL itself (due to Donnan exclusion) to facilitate reaction with water-dissociation-generated H^+. The H^+ from water dissociation exits out of the CEL and reacts with HCO_3^- in the electrolyte to form CO_2 that reaches its solubility limit, becomes saturated, and bubbles out, as is consistent with the experimental visual observation (**Supporting Video S1**) and prior studies of BPMs operated in $KHCO_3$ solutions.[32,34]

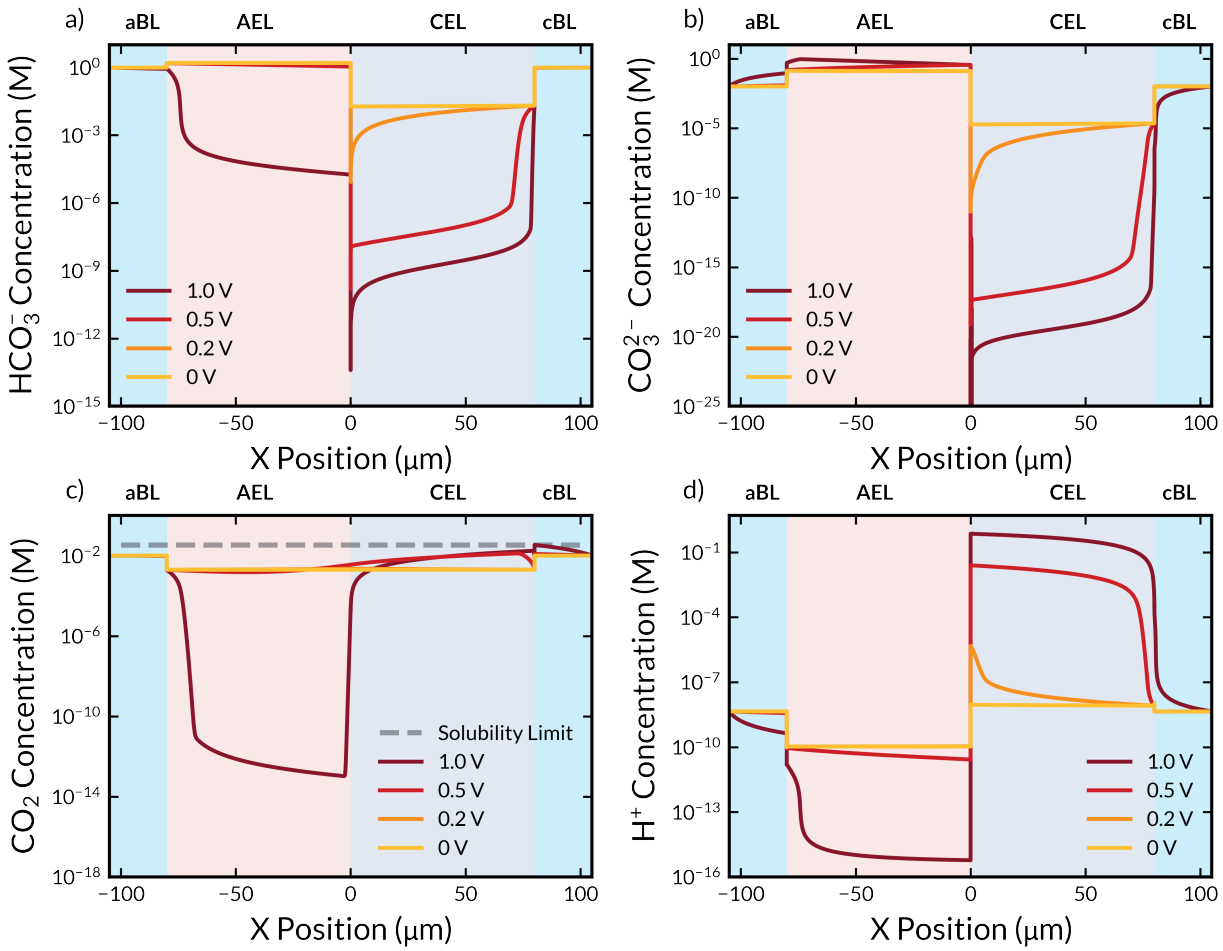

Figure 4: Simulated concentration profiles of **(a)** HCO_3^-, **(b)** CO_3^{2-}, **(c)** dissolved CO_2, and **(d)** H^+ within a BPM immersed in 1 M $KHCO_3$ at applied membrane voltages of 0 V, 0.2 V, 0.5 V, and 1.0 V. Grey-dashed line in panel **(c)** denotes the solubility limit of CO_2 in water. Zoomed plots at the AEL|CEL interface can be found in **Section S8** of the **SI**.

On the AEL side, pH increases do not occur as readily with increasing cell potential, because the AEL is fully (bi)carbonate exchanged at equilibrium and the presence of (bi)carbonates in these high (~1-2 M) concentrations buffer changes in pH and pOH. This is important to note, because the pH gradient in these systems is typically assumed to be directly proportional to the electrostatic potential profiles (**Figure S22-23**).[58] However, these results demonstrate that the weak-acid buffer breaks the scaling relationship between the applied potential and the developed pH gradient by competitively consuming generated OH^- anions.

Nonetheless, past potentials of 0.5 V, the pH does increase within the AEL. Past this potential, the concentration of dissolved CO_2 decreases significantly due to equilibrium reactions with water-dissociation-generated OH^- and is essentially entirely consumed within the AEL. Concurrently, HCO_3^- is consumed to form CO_3^{2-}, so the concentration of HCO_3^- in the AEL decreases, and that of CO_3^{2-} increases at high applied potentials. Once essentially all of the HCO_3^- in the AEL has been consumed (V > 0.7 V), the pH in the AEL increases much more rapid, and the generated OH^- leaves the BPM and reacts with HCO_3^- anions in the anolyte. While the concentration of HCO_3^- in the AEL tends to zero at 1.0 V of applied potential, the concentration remains near the bulk concentration in the electrolyte, demonstrating that there is an abundance of reactive (bi)carbonate to consume water-dissociation-generated OH^- anions. It is important to note that while *in-situ* CO_2 regeneration on the cathode side occurs at the CEL|cBL interface due to exclusion of (bi)carbonates from the CEL, the regeneration of the CO_3^{2-} sorbent from the HCO_3^- occurs within the entirety of the AEL, CL, and anolyte domains. Because HCO_3^- can exchange into the AEL and CL, the direct field-enhanced dissociation of HCO_3^- anions in the CL, as well as the reaction of HCO_3^- with water-dissociation-generated OH^- throughout the CL, AEL, and anolyte, regenerate the CO_3^{2-} carbon capture sorbent.

A similar analysis of concentration profiles was also performed for BPMs immersed in simulated seawater (**Figure S18-21, S24-25**). The model shows very similar behavior as for the 1 M $KHCO_3$ case with respect to the equilibria. However, due to the incredibly low concentrations of reactive carbon in the seawater electrolyte, the BPM is primarily exchanged with Na^+ or Cl^- for the CEL or AEL, respectively. At the CEL side, the catholyte is rapidly mass-transfer limited by HCO_3^-, impeding the formation of CO_2 *via* the *in-situ* regeneration mechanism. However, on the

AEL side, because there is a larger reactive volume of HCO_3^- wherein both the AEL and anolyte contain reactive HCO_3^-, the mass-transport limitations are less severe for the regeneration of the CO_3^{2-}, suggesting that the BPM-ED system for DOC is more effective for mineralization than for CO_2 release.

Lastly, because the equilibrium reactions are key to both the CO_2 and CO_3^{2-} regeneration, the ratio of the local forward and backward rates of each reaction (1)-(5), representing the deviation of these reactions from equilibrium, were plotted throughout the modeled domain for both the 1 M $KHCO_3$ and simulated seawater cases (**Figures S26-S29**). Interestingly, owing to their fast kinetics, reactions (1), (3), and (5) reach equilibrium throughout the entire domain, except for within the CL. However, reactions (2) and (4) significantly deviate from equilibrium within the catholyte where CO_2 regeneration occurs. Indeed, they favor their reverse direction, demonstating that the water dissociation H^+ flux drives these reactions out of equilibrium towards regenerating CO_2. This analysis demonstrates the importance of the BPM pH swing in driving buffer reactions within the ion-conducting polymer domains.

3.3 Simulated Fluxes and Transference Numbers of Ionic Species

While an understanding of the local concentrations and environments within the BPM provides valuable information regarding the phenomena occurring within it, knowledge of the fluxes of the various ionic species in these membranes is just as crucial. The primary charge carrier within an ion-exchange membrane dictates its conductivity,[50,53,59] and understanding charge transport through the BPM is key to mitigating detrimental phenomena such as salt crossover.[27] Plotting the effective transference numbers, defined here as the fraction of current carried by a given

species, of all ions as a function of applied potential throughout the BPM (**Figure 5**; **Figure S30-32**) reveals the nature of charge transport within the BPM operated with 1 M $KHCO_3$. At low applied potentials (0 V and 0.2 V), the current density is primarily due to co-ion crossover (**Figure 5a-b**) (K^+ crossing from the anolyte to catholyte or HCO_3^- crossing from the catholyte to anolyte), with K^+ the dominant carrier of current, due to its higher diffusion coefficient in the BPM.[27]

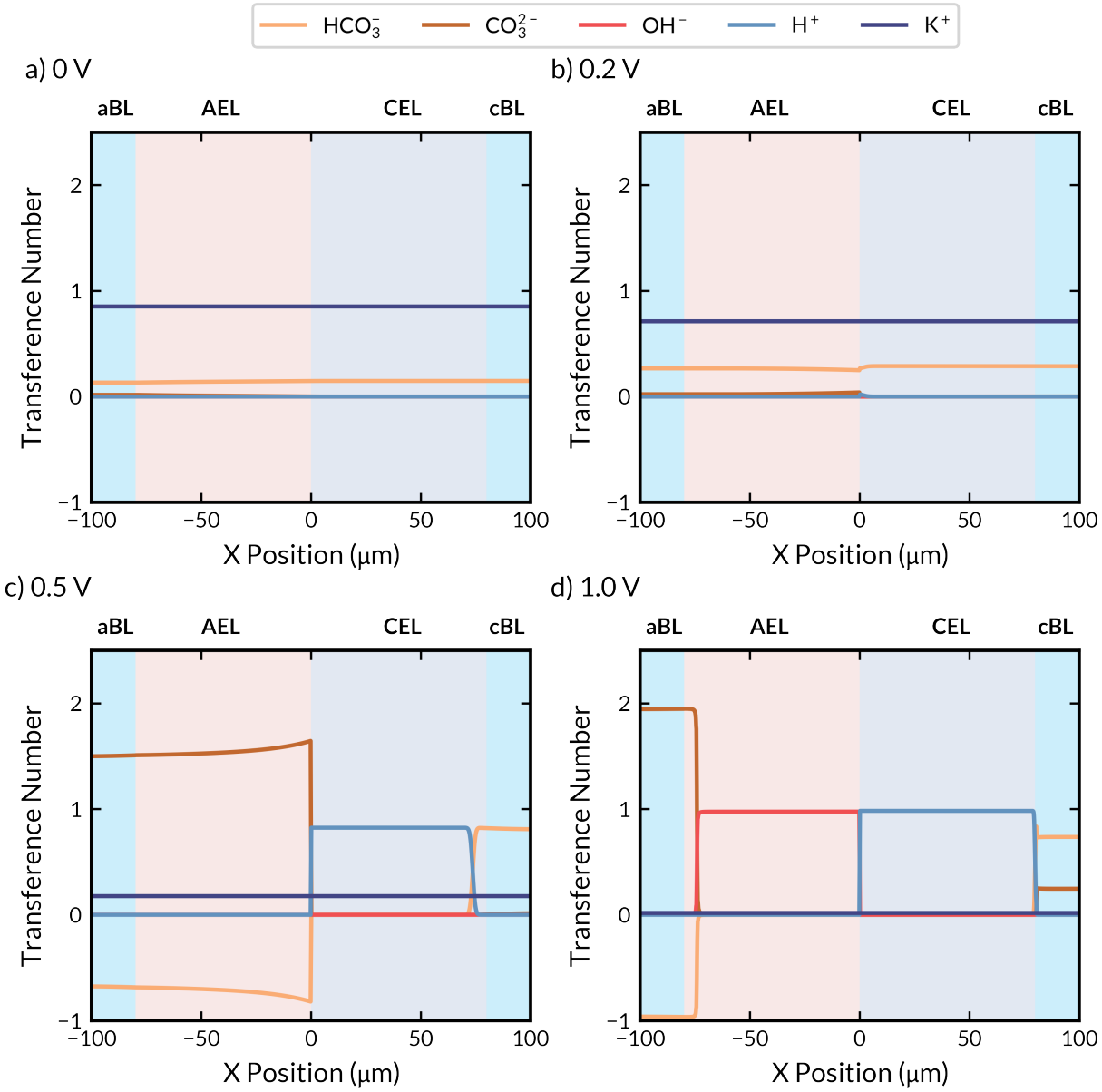

Figure 5: Simulated effective transference-number profiles of HCO_3^-, CO_3^{2-}, H^+, OH^-, and K^+ within a BPM immersed in 1 M $KHCO_3$ at applied membrane voltages of **(a)** 0 V, **(b)** 0.2 V, **(c)** 0.5 V, and **(d)** 1.0 V.

As the applied potential is increased and electric-field-enhanced water dissociation occurs, H^+ rapidly becomes the primary charge carrier in the CEL (**Figure 5c-d**). For the AEL, on the other hand, CO_3^{2-} becomes the primary charge carrier at moderate potentials (0.4 – 0.7 V), and HCO_3^- possesses a negative effective transference number (**Figure 5c**). This flux behavior is consistent with the interpretation that HCO_3^- transports as a counter-ion through the AEL to the CL, where it is either directly dissociated by the large electric field or reacts with water-dissociation-generated OH^- to form CO_3^{2-} that can then transports directly out of the CL and serves as the major carrier of charge in the AEL. At higher potentials (> 0.7 V), where HCO_3^- is depleted, OH^- becomes the primary charge carrier in the AEL (**Figure 5d**). Interestingly, H^+ and OH^- do not immediately become the primary carrier of charge in the BPM when water dissociation begins at ~0.5 V, and there appears to be a penetration depth moving out from the CL through which the fronts of H^+ and OH^- flux dominate. This penetration depth is dependent on the current density and is due to out-of-equilibrium buffer reactions that convert the generated OH^- or H^+ to alternative charge carrying ions within the BPM domain. At large enough current densities, the buffering species within the BPM are depleted, and H^+ and OH^- become the dominant charge carriers throughout the entirety of the BPM. This flux analysis was also carried out for the simulated seawater case and similar trends were observed (**Figures S33-35**). However, due to the small concentration of reactive carbon in the seawater, OH^- and H^+ much more rapidly become the primary charge carriers in the BPM.

Taken together, this knowledge suggests that operation of BPM-ED systems at high current density could be beneficial for several reasons. At higher current densities, salt crossover is less extensive due to the dominance of H^+ and OH^- as charge carriers. Additionally, at these higher current densities, OH^- fully replaces the initially exchanged (bi)carbonates as the charge carrying species in the AEL, which reduces ohmic losses due to the higher mobility of OH^-.[60]

3.4 Energy Intensities and Efficiency of CO_2 Desorption via BPM-ED

Key to any carbon-capture process is understanding the efficiency and energy requirements for operation at various rates. One key promise of EMCC processes is that they could potentially enable lower energy intensities than thermal processes.[2] Thus, the simulation was employed to determine the coulombic efficiency (**Figure *6*a**) and energy intensity (**Figure *6*b**) for CO_2 regeneration as a function of applied current density. Coulombic efficiency is defined as the fraction of the applied current density that goes toward regenerating CO_2 in the catholyte boundary layer and can be thought of as the product of the water dissociation efficiency, and the efficiency of reacting water-dissociation-generated H^+ with HCO_3^- to form CO_2.

For all electrolytes tested (0.5 M $KHCO_3$, 1 M $KHCO_3$, and simulated seawater), the coulombic efficiency initially is 0% due to the dominance of salt-crossover at low current densities. Nonetheless, the efficiency rapidly increases to ~80% for all electrolytes due to the onset of the water dissociation reaction. Crucially, water dissociation in all electrolytes rapidly reaches ~99% efficiency (**Figure S36**), consistent with prior study of the Fumasep BPM, meaning that deviations coulombic efficiencies lower than 99% are due to inefficiencies in conversion of the generated H^+.[40]

For the simulated seawater BPM, the coulombic efficiency monotonically decreases as current density increases. The rapid decrease of coulombic efficiency for simulated seawater is due to complete consumption of the meager 0.00211 M HCO_3^- in the catholyte (*i.e.*, the CO_2 regeneration is HCO_3^- limited). For the simulated seawater, once all the HCO_3^- in the catholyte diffusion boundary layer is consumed, the H^+ flux from the BPM exits the boundary layer unreacted, acidifying the bulk electrolyte. The impact of unreacted H^+ can be seen due to the effective transference number of H^+ in the catholyte reaching 1 at high current densities (**Figure S33**). It is important to note that the coulombic efficiency defined herein is the coulombic efficiency of H^+ liberating CO_2 within the diffusion boundary layer. Unreacted H^+ could theoretically react with further dissolved inorganic carbon to liberate greater amounts of CO_2 by feeding more electrolyte downstream. However, in this work, we seek to consider just the fluxes in the direct vicinity of the BPM to explore the effects of mass transfer at the micrometer scale. This effect may vary near the terminal electrodes in a BPM-ED stack depending on the consumption of protons and hydroxides by the redox reactions.

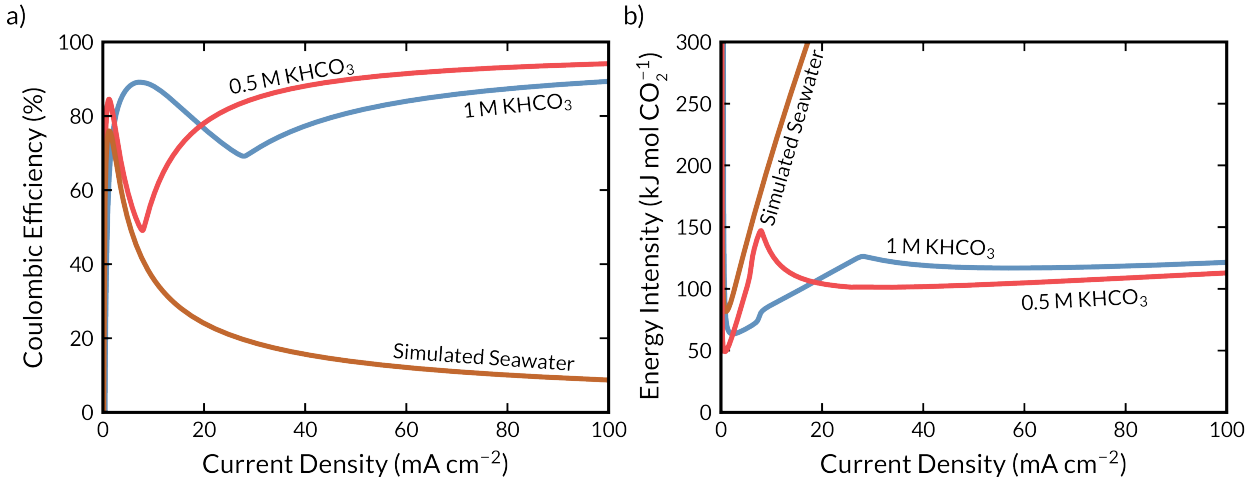

Figure 6: Simulated **(a)** coulombic efficiency and **(b)** energy intensity of BPM-ED for EMCC from 1 M and 0.5 M $KHCO_3$ as well as for DOC in simulated seawater.

For the 0.5 M and 1 M $KHCO_3$ electrolytes, the coulombic efficiency similarly decreases after achieving a maximum of ~80%. However, instead of being HCO_3^- limited, the reduction in coulombic efficiency at intermediate current densities is limited by the consumption of H^+ by CO_3^{2-} to form HCO_3^- (**Figures S38-S39, Section S17**). Once all of the CO_3^{2-} in the catholyte has been consumed, there is an inflection point in the coulombic efficiency at which the CO_2 regeneration increases again, achieving higher coulombic efficiencies approaching 90% for 1 M $KHCO_3$ and 95% for 0.5 M $KHCO_3$ at current densities approaching 100 mA cm^{-2}. The coulombic efficiencies reported in these electrolytes are also consistent with prior work by Eisaman *et al.*[16] Between 0.5 and 1 M $KHCO_3$, 0.5 M $KHCO_3$ possesses a higher coulombic efficiency at high current density due to its lower bulk pH, which inhibits the loss of water dissociation generated H^+ to H^+-OH^- recombination and H^+-CO_3^{2-} recombination relative to the 1 M $KHCO_3$ case. The above analysis demonstrates that the regeneration of CO_2 in the diffusion boundary layer is dictated by complex interactions between H^+, HCO_3^-, and CO_3^{2-} and their associated buffer kinetics.

Considering the energy intensity for these processes, the simulated seawater BPM requires a larger energy intensity at high current densities due to mass-transport limitations associated with the low concentrations of dissolved carbon species and the resulting low coulombic efficiency. However, at low current densities, where the flux is well matched to the concentration of (bi)carbonates, the energy intensity for CO_2 generation by the BPM is < 100 kJ mol CO_2^{-1}. Further, the simulated energy intensity for CO_2 desorption at 3.3 mA cm^{-2} is 108 kJ mol CO_2^{-1}, which agrees quite well with the 155 kJ mol CO_2^{-1} experimental reported by Digdaya *et al.*,[61] when considering the energy requirement in that report included losses associated with a

ferro/ferricyanide redox couple at the working and counter electrodes (~40 kJ mol CO_2^{-1} at an equivalent current density).

Conversely, the 1 and 0.5 M $KHCO_3$ cases possess lower energy intensities due to higher concentrations of HCO_3^- anions in the catholyte boundary layer for reaction, maintaining energy intensities near 100 kJ mol CO_2^{-1} even at current densities of 100 mA cm^{-2}. 0.5 M $KHCO_3$ possesses a lower energy intensity due to its higher coulombic efficiency at high current densities. These energy intensities compare well with thermal processes, and the current densities achieved far exceed those demonstrated for other EMCC processes.[2,23]

The coulombic efficiency of sorbent regeneration, in terms of the transference number for CO_3^{2-} at the anolyte boundary, is nearly 100% for 1 and 0.5 M $KHCO_3$ (**Figure S40-41**). As stated previously, this is likely due to an increased space time for HCO_3^- conversion into CO_3^{2-}. The ability for the AEL to exchange with both HCO_3^- and water-dissociation-generated OH^- enables a high activity for these ions to react and form CO_3^{2-} in the anolyte boundary layer and within the AEL and CL. The buffer reactions in the simulated seawater BPM are still limited by HCO_3^- concentration, but the conversion efficiency remains > 30% at all current densities (**Figure S40-41**).

Lastly, we note that a BPM implemented in a carbon capture loop as shown in **Figure *1***, will likely operate with a gradient in pH and dissolved carbon species, as the electrolyte fed back to anolyte side will be slightly acidified and have some carbon removed. Thus, the simulation was run with a gradient across the BPM in both pH and dissolved inorganic carbon, wherein the catholyte was fed with 1 M $KHCO_3$ (pH = 8.3) as before, but the anolyte was fed with 0.9 M $KHCO_3$ (pH = 7.5) to represent 10% stripping of carbon by BPM-ED and the following CO_2 stripping

process. As shown in **Figure S42-43**, the choice to operate under this gradient has no effect on the energetics or efficiency for CO_2/CO_3^{2-} recovery, except at very low current densities (i < 10 mA cm^{-2}) due to a large diffusive flux at 0 V associated with the imposed concentration gradient across the BPM. All told, the high coulombic efficiencies and low energy intensities (competitive with thermal desorption)[5] demonstrated indicate that BPM-ED possesses promise for application as a carbon-removal technique.

3.5 Effect of CO_2 Bubble Formation on BPM-ED Performance

Management of bubbles is key in the development of electrochemical devices,[55,62,63] and this is especially true for carbon-capture devices that must mediate the generation of CO_2 gas from an aqueous (bi)carbonate electrolyte. Work by Diederichsen *et al.* identified bubble management as a key challenge in continuous EMCC systems due to power losses that occur from loss of electrochemically active surface area due to CO_2 bubbling.[12] The model presented here enables a simulation of the bubble coverage on the CEL, as well as an understanding of how the bubble coverage affects the energy requirements for BPM-ED EMCC.

First, it is important to note that due to mass-transport limitations in the seawater case as discussed above, bubbling only occurs for the BPMs exchanged with $KHCO_3$. Analysis of the bubble coverage in these simulations (**Figure 7a**) shows that the bubble coverage of the BPM exceeds 30% at high current densities due to super saturation of the electrolyte. This high bubble coverage is consistent with visual observation of the CEL during operation (**Supporting Video S1**). Additionally, the analysis of the energy requirements with and without losses due to bubble coverage reveals that bubble effects account for nearly 10 kJ mol^{-1} of energy loss (**Figure 7b**) for both $KHCO_3$ cases at 100 mA cm^{-2}. Therefore, managing bubbles is indeed crucial to improving

energy efficiencies for BPM-ED EMCC. Previous knowledge from water electrolysis shows that bubble coverage losses can be ameliorated by controlling flow rate, increasing gas headspace pressure,[64] or by employing a surfactant to reduce surface tension and bubble size.[65,66] The BPM morphology and surface chemistry can also be modulated to alter the wettability and coverage of bubbles on the surface.

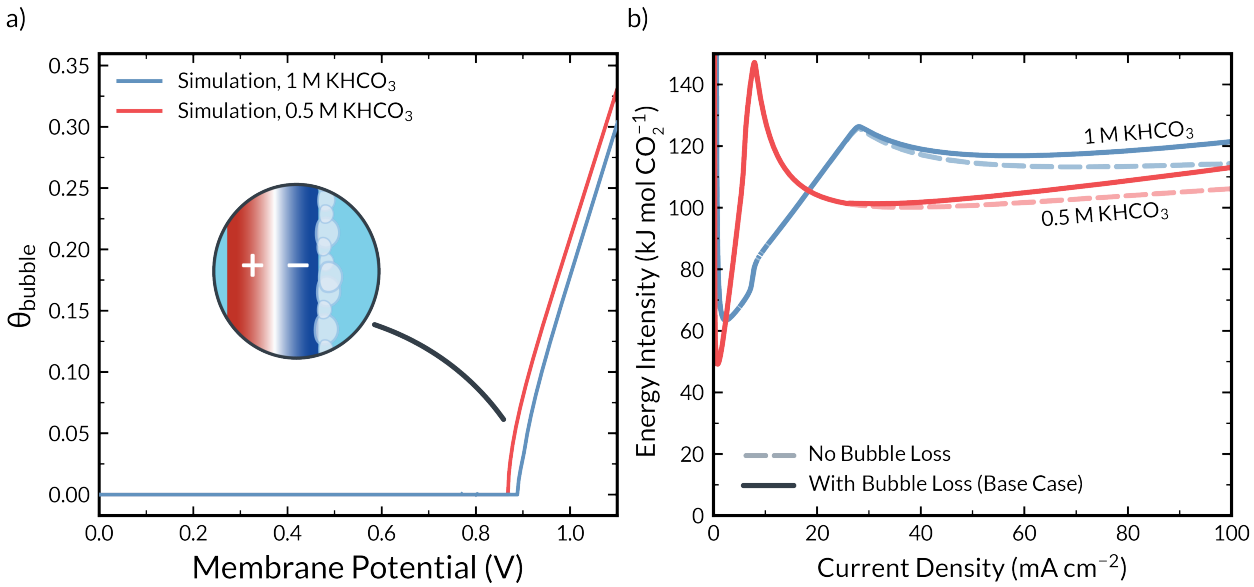

Figure 7: Effect of CO_2 bubble formation on energetic penalties in BPM-ED EMCC. **(a)** Simulated bubble coverage as a function of applied membrane potential. **(b)** Simulated energy intensity of a BPM with no bubble management (solid lines) and perfect bubble management (dashed lines).

The effect of flow rate can be represented in our model through the thickness of the anolyte and catholyte diffusion boundary layers. Lower flow rates are represented by thicker boundary layers, and higher flow rates are represented by thinner boundary layers.[67] As shown in **Figure S44-S45**, changing the flow rate has little effect on the polarization curve when deconvoluting bubble induced surface area losses (*i.e.,* flow rate has no impact on the base BPM energy requirement) or the overall rate of CO_2 flux from the catholyte. However, increasing flowrate does increase the onset current density for which bubbling is observed, reducing bubble coverage. At the basecase boundary-layer thickness of 25 μm (corresponding to a Reynolds

number (Re) of 18,000, which is in the laminar flow regime over a smooth flat plate[68]), bubbling occurs at a current density of approximately 20 mA $cm^{-2,}$ consistent with experiment. However, for a boundary-layer thickness of 10 μm (corresponding to Re of 111,000, still in the laminar flow regime for a flat plate[68]), bubbling does not occur until 60 mA cm^{-2}. The delay on the onset of bubbling occurs because the faster transport of CO_2 away from the reactive cBL|CEL boundary prevents supersaturation and keeps CO_2 dissolved within the aqueous electrolyte.

To highlight the importance of bubble management, further experiments were performed. In these studies, the BPM-ED system was run with various electrolyte flowrates, and the extent of CO_2 bubbling was quantified by determining the noise in the measured electrostatic potential as calculated by the standard deviation in the measured transmembrane potential (details on these experiments can be found in **Section S21**). **Figure S47a** compares standard deviation of potential as a function of applied current density for three different flow rates (0.2, 1, and 5 mL min^{-1}). As shown in the figure, the extent of bubbling is much more severe for lower flowrates, and the onset of bubbling occurs at lower current densities, as predicted from the model.

Figures S48a and S48b depict polarization curves for Fumasep tested at each flow rate in 1 M $KHCO_3$ and 0.5 M NaCl, respectively. Comparing the two plots indicates that the addition of bicarbonate species into the electrolyte increases the average voltage measured at each current density. Furthermore, without the bicarbonate species present (**Figure S48b**), flowrate has no effect of the measured BPM voltage, signifying that flowrate dependence is only introduced once the bicarbonate is added to induce CO_2 bubble formation, in agreement with the simulations. Indeed, in the presence of bicarbonate (**Figure S48a**), the average voltage is highest for the lowest

flowrate, indicating that an increase in bubble coverage under reduced flows leads to decreased surface area and increased resistance. This experimental data further supports the importance of flowrate and bubble mitigation on maintaining low cell voltages when operating BPMs for carbon removal due to the surface area losses driven by CO_2 bubble formation on membrane surfaces.

3.6 Applied-Voltage-Breakdown Analysis for BPM-ED EMCC

Because the energetic requirements of BPM-ED EMCC are critical to the optimization and implementation of these systems, voltage contribution analysis[69] of the BPM operating in 1 M $KHCO_3$ and simulated seawater were conducted to determine the major sources of power loss in the BPM-ED system. As expected, the thermodynamic potential required to drive the pH gradient across the CL via electric-field enhanced water dissociation (**Section S1.2**) makes up the largest contribution to the applied potential. The next largest potential loss in the system is the kinetic overpotential for the water dissociation in the CL (**Section S1.2**). Unfortunately, while the thermodynamic requirements cannot be altered, the kinetic overpotential can be lowered by employing a better water-dissociation catalyst.[26,42] For the 1 M $KHCO_3$ case, bubble coverage losses also make up a significant portion of the applied potential, particularly at high current densities, and those could be managed by better controlling flow as discussed in section 3.5 or through other bubble-mitigation strategies. Lastly, ohmic losses through the CEL and AEL are quite low relative to other losses, but do increase with current density and will likely become critical if the BPM-ED system is to operate at currents approaching 1 A cm^{-2}. Although minor, these losses can be decreased by improving ionic conductivity of the AEL and CEL. This applied-voltage breakdown highlights that the greatest areas for improvement in the BPM-ED

performance are in improving the water dissociation catalyst and in implementing bubble-management strategies.

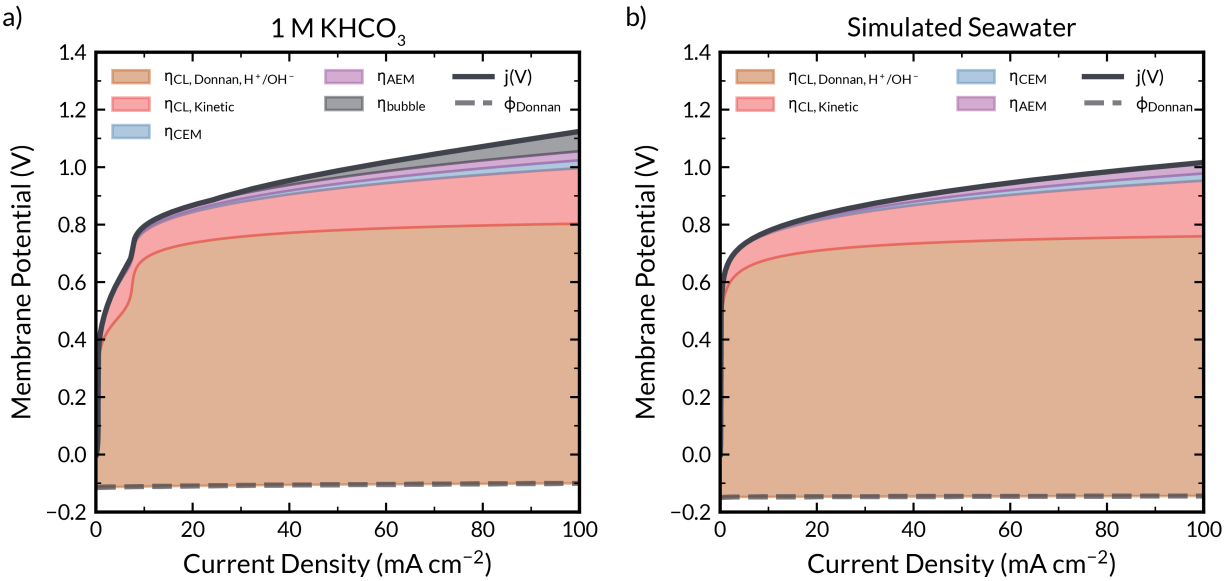

Figure 8: Applied-voltage breakdown for a BPM immersed in **(a)** 1 M $KHCO_3$ and **(b)** simulated seawater.

3.7 Sensitivity Analysis of BPM-ED EMCC

Sensitivity analysis was performed on the BPM-ED simulations to better understand the effect of BPM and CL properties on the performance of the BPMs immersed in reactive carbon solutions. For the following sensitivity analyses, the effects of bubble coverage are not considered, essentially assuming that a bubble mitigation strategy has been developed and implemented. Prior studies have demonstrated that the increase of the ion-exchange capacity (IEC) or fixed-charge in the BPM can enhance the rate of water dissociation by increasing the electric field between the AEL and CEL.[26,49] As shown in **Figures S50-S51**, increasing the IEC does indeed improve the rate of water dissociation significantly, and consequently the rate of CO_2 flux at a given applied potential. Improving the performance of the water-dissociation catalyst has also been proven to be key in reducing energy requirements for BPM operation.[42,70] As such, the model

was run with varying values of α_{WD}, which represents the sensitivity of water dissociation to the electric field. The results show that performance of the BPM in reactive carbon solutions is indeed incredibly sensitive to the catalyst activity (**Figure S52**). Taken together, these results indicate that improving bubble removal from the BPM surface, increasing the IEC of the ionomers, and using a better WD catalyst would drastically enhance the performance of BPM-ED EMCC.

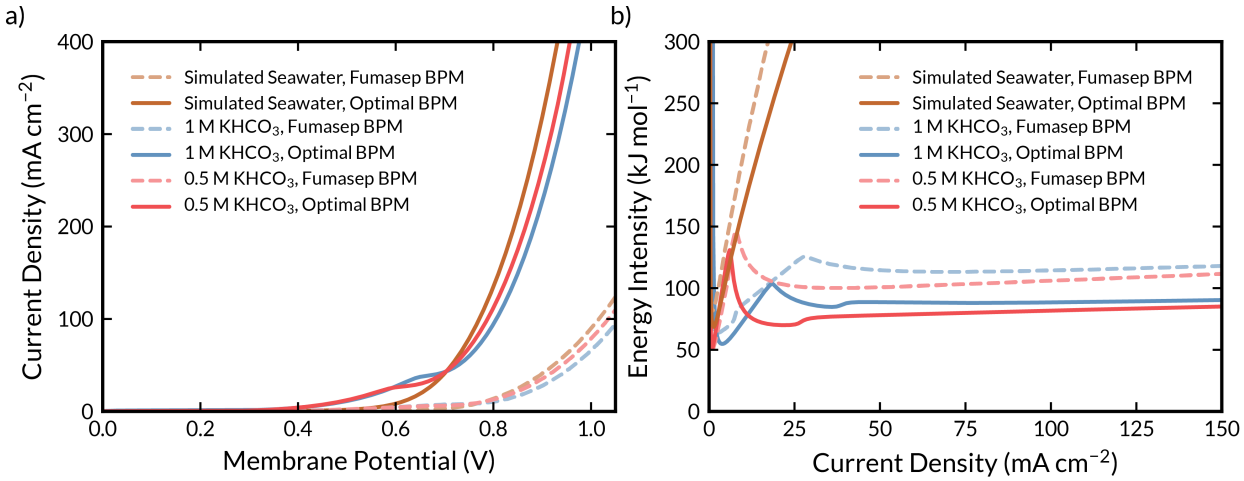

Figure 9: Sensitivity analysis of BPM polarization curves in various EMCC solutions. **(a)** Sensitivity of polarization curve to BPM properties. **(b)** Sensitivity of energy intensity to BPM properties.

Recent work by Pintauro *et al.* demonstrated a BPM meeting these criteria, employing a BPM with a high fixed-charge concentration and a complex 3-D junction CL for efficient water dissociation in a 0.5 M Na_2SO_4 electrolyte.[71] Parameters in the model were fit in order for the simulation to match observed performance by Pintauro in 0.5 M Na_2SO_4 (**Section S22.1**) and the performance of the "Optimal BPM" in reactive carbon capture solutions was simulated. As shown in **Figure 9a**, employing the optimal BPM dramatically improves the polarization behavior compared to the Fumasep BPM employed in this study. More promising, however, is that the use of the Optimal BPM substantially lowers the energy intensity for CO_2 desorption well below 100 kJ mol CO_2^{-1}, even at current densities at or exceeding 100 mA cm^{-2} for the 0.5 and 1 M $KHCO_3$

electrolytes. Applied-voltage breakdowns (**Figure S54**) demonstrate that these improvements are due to improved ionic conductivity due to the enhanced IEC, as well as significantly reduced overpotentials for water dissociation due to the high IEC and improved catalytic behavior, and the assumed mitigation of bubble losses in the system.

The above calculations correspond to the energy intensity of a single BPM unit in an overall stack, and the number of BPMs in the stack will be key to dictating efficiency, especially when considering the electrode potentials of the anode and cathode. As shown in **Figure S55**, considering the effect of the anode and cathode potentials does increase the energy intensity of the process quite significantly (from 88 kJ mol CO_2^{-1} to 176 kJ mol CO_2^{-1} at 100 mA cm^{-2}). However, as the number of BPMs in the stack increases, the energy intensity rapidly approaches that of the single BPM unit simulated herein. For a BPM-ED stack containing ten of the Optimal BPMs, the theoretical energy intensity is still below 100 kJ mol CO_2^{-1} at 100 mA cm^{-2} (see **Section S24** for the details of this calculation). Ultimately, this analysis reveals the exciting result that newly developed BPMs have achieved such substantial strides in water-dissociation catalysis that CO_2 desorption via BPM-ED could be achieved at energy intensities lower than 100 mA cm^{-2} even for current densities exceeding 100 mA cm^{-2}, making this technology quite promising for carbon removal when considered in a BPM-ED stack configuration.

4. Conclusions

Electrochemically mediated carbon capture strategies have the potential to displace thermal desorption techniques due to their ability to operate with lower energy requirements at ambient temperatures and pressure. Bipolar-membrane electrodialysis (BPM-ED) is a promising

technique that uses the H^+ and OH^- fluxes generated by electric-field-enhanced water dissociation in the BPM to drive the release of CO_2 and the recovery of CO_3^{2-} from an electrolyte containing reactive carbon species simultaneously. Herein, we developed simulations, which closely match experiments, and resolved the rates of the various kinetic and transport processes (field enhanced water or bicarbonate dissociation, homogeneous buffer reactions, salt crossover, *etc.*) occurring within BPMs immersed in three reactive carbon solutions relevant to carbon capture: 1 M $KHCO_3$, 0.5 M $KHCO_3$, and simulated seawater. Simulations reveal that an early onset in observed current density for (bi)carbonate exchanged BPMs is due to field enhanced dissociation of the bicarbonate anions as well as a reduction in H+-OH- recombination due to competitive reaction of OH- with HCO_3^- to form CO_3^{2-} indirectly.

Local concentrations and fluxes in the BPM from the simulations elucidated that alkali cations and (bi)carbonates are the dominant ion and primary charge carrier in the BPM at low current densities, with water-dissociation generated H^+ and OH^- becoming the dominant ions at high current densities once buffering (bi)carbonate anions are consumed by homogeneous reaction. Furthermore, the energy intensity for CO_2 desorption as a function of applied current density is also determined, for which the model reveals that the low concentration of (bi)carbonates in simulated seawater leads to mass-transport limitations and consequently high energy intensities for CO_2 recovery at high current densities for BPMs immersed in seawater. Conversely, BPMs in higher concentrations of (bi)carbonates do not become mass-transport limited for CO_2 recovery up to 100 mA cm^{-2}, and can achieve energy intensities competitive with thermal desorption of approximately 100 kJ mol^{-1} at current densities far exceeding those demonstrated for other EMCC processes. Lastly, analysis of the losses in the system revealed that

the greatest opportunities for optimization of these systems are through the management of CO_2 bubbles and the improvement of the water-dissociation catalyst. Simulating a BPM with bubble-mitigation strategies and a substantially enhanced water dissociation catalyst (consistent with the state-of-the-art BPM in literature) shows that these improvements enable performance for BPM-ED EMCC at 100 mA cm^{-2} at energy intensities well below 100 kJ mol CO_2^{-1}. Ultimately, this work provides substantial insight into the mechanistic behavior of reactive carbon species in BPM systems, relevant to many electrochemical systems across the gamut of carbon-capture and -conversion technologies, and elucidates the promise of BPMs in performing BPM-ED for carbon capture at current densities exceeding 100 mA cm^{-2}.

5. Acknowledgements

This material is based on work performed within the Liquid Sunlight Alliance, which is supported by the U.S. Department of Energy, Office of Science, Office of Basic Energy Sciences, Fuels from Sunlight Hub under Award Number DE-SC0021266. JCB would like to acknowledge support from the National Defense Science and Engineering Graduate Fellowship (NDSEG) supported by the Army Research Office (ARO). The authors would also like to acknowledge Prof. Shane Ardo for helpful discussions regarding the effect of the electric field on the (bi)carbonate anions.

6. Nomenclature

Roman

a_i	Activity of species i
c_i	Concentration of species i (M)
D_i	Diffusivity of species i ($m^2\ s^{-1}$)
E	Electric field ($V\ m^{-1}$)
f_i	Activity coefficient of species i
F	Faraday constant ($C\ mol^{-1}$)
G	Gibbs free energy ($J\ mol^{-1}$)
IEC	Ion Exchange capacity ($mmol\ g^{-1}$)
k_B	Boltzmann constant ($J\ K^{-1}$)
K_n	Equilibrium constant in reaction n
k_n	Forward rate constant of reaction n ($m^3\ s^{-1}\ mol^{-1}$)
L	Length (m)
l_B	Bjerrum Length (m)
M_i	Molar mass of species i ($g\ mol^{-1}$)
N_i	Molar flux of species i ($mol\ m^{-2}\ s^{-1}$)
R	Ideal gas constant ($J\ mol^{-1}\ K^{-1}$)
$R_{B.i}$	Source term for species i ($mol\ m^{-3}\ s^{-1}$)
$s_{i,n}$	Stoichiometric coefficient of species i in reaction n
T	Temperature (K)
x	1-dimensional position variable (m)
z_i	Charge of ion i

Greek

β	Non-dimensional electric field scaling factor (m V^{-1})
ε	Dielectric permittivity (F m^{-1})
λ	Water content
μ	Chemical potential of species i (J mol^{-1})
ξ	Species-membrane/Species-water diffusivity ratio
ρ	Density (g cm^{-3})
σ	Dimensionless dissociation bond length
Φ	Electrostatic potential (V)
ε_k	Volume fraction of phase k

Subscript

char	Characteristic
eff	Effective
i	Ionic species
M	Value in membrane
w	Value in water

Superscript

0	Intrinsic value or standard state
E	Electric field dependence

Acronyms

aBL	Anolyte boundary layer

AEL	Anion exchange layer
BPM	Bipolar membrane
BPM-ED	Bipolar membrane electrodialysis
cBL	Catholyte boundary layer
CEL	Cation exchange layer
CL	Catalyst layer
EMCC	Electrochemically-mediated carbon capture
WD	Water dissociation

7. References

(1) IPCC. *Climate Change 2014 Mitigation of Climate Change - Working Group III Contribution to the Fifth Assessment of the Intergovernmental Panel on Climate Change*; 2014.

(2) Liu, Y.; Lucas, É.; Sullivan, I.; Li, X.; Xiang, C. Challenges and Opportunities in Continuous Flow Processes for Electrochemically Mediated Carbon Capture. *iScience* **2022**, *25* (10), 105153.

(3) MacDowell, N.; Florin, N.; Buchard, A.; Hallett, J.; Galindo, A.; Jackson, G.; Adjiman, C. S.; Williams, C. K.; Shah, N.; Fennell, P. An Overview of CO_2 Capture Technologies. *Energy Environ. Sci.* **2010**, *3* (11), 1645–1669.

(4) Keith, D. W.; Holmes, G.; St. Angelo, D.; Heidel, K. A Process for Capturing CO_2 from the Atmosphere. *Joule* **2018**, *2* (8), 1573–1594.

(5) Van Straelen, J.; Geuzebroek, F. The Thermodynamic Minimum Regeneration Energy Required for Post-Combustion CO_2 Capture. *Energy Procedia* **2011**, *4*, 1500–1507.

(6) Gurkan, B.; Su, X.; Klemm, A.; Kim, Y.; Mallikarjun Sharada, S.; Rodriguez-Katakura, A.; Kron, K. J. Perspective and Challenges in Electrochemical Approaches for Reactive CO_2 Separations. *iScience* **2021**, *24* (12), 103422.

(7) Digdaya, I. A.; Sullivan, I.; Lin, M.; Han, L.; Cheng, W. H.; Atwater, H. A.; Xiang, C. A Direct Coupled Electrochemical System for Capture and Conversion of CO_2 from Oceanwater. *Nat. Commun.* **2020**, *11* (1), 1–10.

(8) Sullivan, I.; Goryachev, A.; Digdaya, I. A.; Li, X.; Atwater, H. A.; Vermaas, D. A.; Xiang, C.

Coupling Electrochemical CO_2 Conversion with CO_2 Capture. *Nat. Catal.* **2021**, *4* (11), 952–958.

(9) Sharifian, R.; Wagterveld, R. M.; Digdaya, I. A.; Xiang, C.; Vermaas, D. A. Electrochemical Carbon Dioxide Capture to Close the Carbon Cycle. *Energy Environ. Sci.* **2021**, *14* (2), 781–814.

(10) Seo, H.; Hatton, T. A. Electrochemical Direct Air Capture of CO_2 Using Neutral Red as Reversible Redox-Active Material. *Nat. Commun.* **2023**, *14* (1), 1–11.

(11) Li, X.; Zhao, X.; Liu, Y.; Hatton, T. A.; Liu, Y. Redox-Tunable Lewis Bases for Electrochemical Carbon Dioxide Capture. *Nat. Energy* **2022**, *7* (11), 1065–1075.

(12) Diederichsen, K. M.; Liu, Y.; Ozbek, N.; Seo, H.; Hatton, T. A. Toward Solvent-Free Continuous-Flow Electrochemically Mediated Carbon Capture with High-Concentration Liquid Quinone Chemistry. *Joule* **2022**, *6* (1), 221–239.

(13) Clarke, L. E.; Leonard, M. E.; Hatton, T. A.; Brushett, F. R. Thermodynamic Modeling of CO_2 Separation Systems with Soluble, Redox-Active Capture Species. *Ind. Eng. Chem. Res.* **2022**, *61* (29), 10531–10546.

(14) Liu, Y.; Ye, H. Z.; Diederichsen, K. M.; Van Voorhis, T.; Hatton, T. A. Electrochemically Mediated Carbon Dioxide Separation with Quinone Chemistry in Salt-Concentrated Aqueous Media. *Nat. Commun.* **2020**, *11* (1), 1–11.

(15) Rahimi, M.; Khurram, A.; Hatton, T. A.; Gallant, B. Electrochemical Carbon Capture Processes for Mitigation of CO_2 Emissions. *Chem. Soc. Rev.* **2022**, *51* (20), 8676–8695.

(16) Eisaman, M. D.; Alvarado, L.; Larner, D.; Wang, P.; Garg, B.; Littau, K. A. CO_2 Separation Using Bipolar Membrane Electrodialysis. *Energy Environ. Sci.* **2011**, *4* (4), 1319–1328.

(17) Eisaman, M. D.; Alvarado, L.; Larner, D.; Wang, P.; Littau, K. A. CO_2 Desorption Using High-Pressure Bipolar Membrane Electrodialysis. *Energy Environ. Sci.* **2011**, *4* (10), 4031–4037.

(18) Stern, M. C.; Simeon, F.; Herzog, H.; Hatton, T. A. Post-Combustion Carbon Dioxide Capture Using Electrochemically Mediated Amine Regeneration. *Energy Environ. Sci.* **2013**, *6* (8), 2505–2517.

(19) Rheinhardt, J. H.; Singh, P.; Tarakeshwar, P.; Buttry, D. A. Electrochemical Capture and Release of Carbon Dioxide. *ACS Energy Lett.* **2017**, *2* (2), 454–461.

(20) Diederichsen, K. M.; Liu, Y.; Ozbek, N.; Seo, H.; Hatton, T. A. Toward Solvent-Free Continuous-Flow Electrochemically Mediated Carbon Capture with High-Concentration Liquid Quinone Chemistry. *Joule* **2022**, *6* (1), 221–239.

(21) Wang, M.; Herzog, H. J.; Hatton, T. A. CO_2 Capture Using Electrochemically Mediated Amine Regeneration. *Ind. Eng. Chem. Res.* **2020**, *59* (15), 7087–7096.

(22) Rahimi, M.; Diederichsen, K. M.; Ozbek, N.; Wang, M.; Choi, W.; Hatton, T. A. An Electrochemically Mediated Amine Regeneration Process with a Mixed Absorbent for Postcombustion CO_2 Capture. *Environ. Sci. Technol.* **2020**, *54* (14), 8999–9007.

(23) Muroyama, A. P.; Pătru, A.; Gubler, L. Review—CO_2 Separation and Transport via Electrochemical Methods . *J. Electrochem. Soc.* **2020**, *167* (13), 133504.

(24) Gurkan, B.; Su, X.; Klemm, A.; Kim, Y.; Mallikarjun Sharada, S.; Rodriguez-Katakura, A.; Kron, K. J. Perspective and Challenges in Electrochemical Approaches for Reactive CO_2 Separations. *iScience* **2021**, *24* (12), 103422.

(25) Iizuka, A.; Hashimoto, K.; Nagasawa, H.; Kumagai, K.; Yanagisawa, Y.; Yamasaki, A. Carbon Dioxide Recovery from Carbonate Solutions Using Bipolar Membrane Electrodialysis. *Sep. Purif. Technol.* **2012**, *101*, 49–59.

(26) Bui, J. C.; Corpus, K. R. M.; Bell, A. T.; Weber, A. Z. On the Nature of Field Enhanced Water Dissociation in Bipolar Membranes. *J. Phys. Chem. C* **2021**, *125* (45), 24974–24987.

(27) Bui, J. C.; Digdaya, I.; Xiang, C.; Bell, A. T.; Weber, A. Z. Understanding Multi-Ion Transport Mechanisms in Bipolar Membranes. *ACS Appl. Mater. Interfaces* **2020**, acsami.0c12686.

(28) Lees, E. W.; Liu, A.; Bui, J. C.; Ren, S.; Weber, A. Z.; Berlinguette, C. P. Electrolytic Methane Production from Reactive Carbon Solutions. *ACS Energy Lett.* **2022**, 1712–1718.

(29) Sharifian, R.; Boer, L.; Wagterveld, R. M.; Vermaas, D. A. Oceanic Carbon Capture through Electrochemically Induced in Situ Carbonate Mineralization Using Bipolar Membrane. *Chem. Eng. J.* **2022**, *438* (February), 135326.

(30) Nagasawa, H.; Yamasaki, A.; Iizuka, A.; Kumagai, K.; Yanagisawa, Y. A New Recovery Process of Carbon Dioxide from Alkaline Carbonate Solution via Electrodialysis. *AIChE J.* **2009**, *55* (12), 3286–3293.

(31) Sharifian, R.; Boer, L.; Wagterveld, R. M.; Vermaas, D. A. Oceanic Carbon Capture through

Electrochemically Induced in Situ Carbonate Mineralization Using Bipolar Membrane. *Chem. Eng. J.* **2022**, *438* (February), 135326.

(32) Li, T.; Lees, E. W.; Goldman, M.; Salvatore, D. A.; Weekes, D. M.; Berlinguette, C. P. Electrolytic Conversion of Bicarbonate into CO in a Flow Cell. *Joule* **2019**, *3* (6), 1487–1497.

(33) Fink, A. G.; Lees, E. W.; Zhang, Z.; Ren, S.; Delima, R. S.; Berlinguette, C. P. Impact of Alkali Cation Identity on the Conversion of HCO_3^- to CO in Bicarbonate Electrolyzers. *ChemElectroChem* **2021**, *8* (11), 2094–2100.

(34) Lees, E. W.; Goldman, M.; Fink, A. G.; Dvorak, D. J.; Salvatore, D. A.; Zhang, Z.; Loo, N. W. X.; Berlinguette, C. P. Electrodes Designed for Converting Bicarbonate into CO. *ACS Energy Lett.* **2020**, *5* (7), 2165–2173.

(35) Sabatino, F.; Gazzani, M.; Gallucci, F.; Van Sint Annaland, M. Modeling, Optimization, and Techno-Economic Analysis of Bipolar Membrane Electrodialysis for Direct Air Capture Processes. *Ind. Eng. Chem. Res.* **2022**, *61* (34), 12668–12679.

(36) Sabatino, F.; Mehta, M.; Grimm, A.; Gazzani, M.; Gallucci, F.; Kramer, G. J.; Van Sint Annaland, M. Evaluation of a Direct Air Capture Process Combining Wet Scrubbing and Bipolar Membrane Electrodialysis. *Ind. Eng. Chem. Res.* **2020**, *59* (15), 7007–7020.

(37) Kas, R.; Yang, K.; Yewale, G. P.; Crow, A.; Burdyny, T.; Smith, W. A. Modeling the Local Environment within Porous Electrode during Electrochemical Reduction of Bicarbonate. *Ind. Eng. Chem. Res.* **2022**.

(38) Lees, E. W.; Bui, J. C.; Song, D.; Weber, A. Z.; Berlinguette, C. P. Continuum Model to

Define the Chemistry and Mass Transfer in a Bicarbonate Electrolyzer. *ACS Energy Lett.* **2022**, *7*, 834–842.

(39) Blommaert, M. A.; Sharifian, R.; Shah, N. U.; Nesbitt, N. T.; Smith, W. A.; Vermaas, D. A. Orientation of a Bipolar Membrane Determines the Dominant Ion and Carbonic Species Transport in Membrane Electrode Assemblies for CO_2 Reduction. *J. Mater. Chem. A* **2021**, *9* (18), 11179–11186.

(40) Blommaert, M. A.; Verdonk, J. A. H.; Blommaert, H. C. B.; Smith, W. A.; Vermaas, D. A. Reduced Ion Crossover in Bipolar Membrane Electrolysis via Increased Current Density, Molecular Size and Valence. *ACS Appl. Energy Mater.* **2020**, *Just Accep*.

(41) Zabolotskii, V. I.; Utin, S. V.; Lebedev, K. A.; Vasilenko, P. A.; Shel'Deshov, N. V. Study of PH Correction Process of Chloride-Bicarbonate Dilute Solutions by Electrodialysis with Bipolar Membranes. *Russ. J. Electrochem.* **2012**, *48* (7), 767–772.

(42) Oener, S. Z.; Foster, M. J.; Boettcher, S. W. Accelerating Water Dissociation in Bipolar Membranes and for Electrocatalysis. *Science (80-.).* **2020**, eaaz1487.

(43) Lucas, É.; Han, L.; Sullivan, I.; Atwater, H. A.; Xiang, C. Measurement of Ion Transport Properties in Ion Exchange Membranes for Photoelectrochemical Water Splitting. *Front. Energy Res.* **2022**, *10* (September), 1–11.

(44) Craig, N. P.; Newman, J. Electrochemical Behavior of Bipolar Membranes, University of California, Berkeley, 2013, Vol. Doctorate.

(45) Newman, J.; Thomas-Alyea, K. E. *Electrochemical Systems*, 3rd ed.; John Wiley and Sons,

Inc.: Hoboken, NJ, 2004.

(46) Onsager, L.; Fuoss, R. M. Irreversible Processes in Electrolytes. Diffusion, Conductance, and Viscous Flow in Arbitrary Mixtures of Strong Electrolytes. *J. Phys. Chem.* **1932**, *36* (11), 2689–2778.

(47) Onsager, L. Deviations from Ohm's Law in Weak. *J. Chem. Phys.* **1934**, *2* (May 1934), 599–615.

(48) Kaiser, V.; Bramwell, S. T.; Holdsworth, P. C. W.; Moessner, R. Onsager's Wien Effect on a Lattice. *Nat. Mater.* **2013**, *12*, 1033–1037.

(49) Lin, M.; Digdaya, I. A.; Xiang, C. Modeling the Electrochemical Behavior and Interfacial Junction Profiles of Bipolar Membranes at Solar Flux Relevant Operating Current Densities. *Sustain. Energy Fuels* **2021**.

(50) Crothers, A. R.; Darling, R. M.; Kusoglu, A.; Radke, C. J.; Weber, A. Z. Theory of Multicomponent Phenomena in Cation-Exchange Membranes: Part II. Transport Model and Validation. *J. Electrochem. Soc.* **2020**, *167* (1), 013548.

(51) Crothers, A. R.; Darling, R. M.; Kushner, D. I.; Perry, M. L.; Weber, A. Z. Theory of Multicomponent Phenomena in Cation-Exchange Membranes: Part III. Transport in Vanadium Redox-Flow-Battery Separators. *J. Electrochem. Soc.* **2020**, *167* (1).

(52) Lucas, É.; Bui, J. C.; Hwang, M.; Wang, K.; Bell, A. T.; Weber, A. Z.; Ardo, S.; Atwater, H. A.; Xiang, C. Asymmetric Bipolar Membrane for High Current Density Electrodialysis Operation with Exceptional Stability. *Chemrxiv* **2023**, 1–33.

(53) Grew, K. N.; Chiu, W. K. S. A Dusty Fluid Model for Predicting Hydroxyl Anion Conductivity in Alkaline Anion Exchange Membranes. *J. Electrochem. Soc.* **2010**, *157* (3), B327.

(54) Mareev, S. A.; Evdochenko, E.; Wessling, M.; Kozaderova, O. A.; Niftaliev, S. I.; Pismenskaya, N. D.; Nikonenko, V. V. A Comprehensive Mathematical Model of Water Splitting in Bipolar Membranes: Impact of the Spatial Distribution of Fixed Charges and Catalyst at Bipolar Junction. *J. Memb. Sci.* **2020**, *603*, 118010.

(55) Liu, J.; Kang, Z.; Li, D.; Pak, M.; Alia, S. M.; Fujimoto, C.; Bender, G.; Kim, Y. S.; Weber, A. Z. Elucidating the Role of Hydroxide Electrolyte on Anion-Exchange-Membrane Water Electrolyzer Performance. *J. Electrochem. Soc.* **2021**, *168* (5), 054522.

(56) Craig, N. P. Electrochemical Behavior of Bipolar Membranes. **2013**.

(57) Dinh, H. Q.; Toh, W. L.; Chu, A. T.; Surendranath, Y. Neutralization Short-Circuiting with Weak Electrolytes Erodes the Efficiency of Bipolar Membranes. *ACS Appl. Mater. Interfaces* **2022**.

(58) Vermaas, D. A.; Wiegman, S.; Smith, W. A. Ion Transport Mechanisms in Bipolar Membranes for (Photo)Electrochemical Water Splitting. *Sustain. Energy Fuels* **2018**, No. 9, 2006–2015.

(59) Kusoglu, A.; Weber, A. Z. New Insights into Perfluorinated Sulfonic-Acid Ionomers. *Chem Rev* **2017**, *117* (3), 987–1104.

(60) Peng, J.; Roy, A. L.; Greenbaum, S. G.; Zawodzinski, T. A. Effect of CO_2 Absorption on Ion

and Water Mobility in an Anion Exchange Membrane. *J. Power Sources* **2018**, *380* (November 2017), 64–75.

(61) Digdaya, I. A.; Sullivan, I.; Lin, M.; Han, L.; Cheng, W. H.; Atwater, H. A.; Xiang, C. A Direct Coupled Electrochemical System for Capture and Conversion of CO_2 from Oceanwater. *Nat Commun* **2020**, *11* (1), 4412.

(62) Hodges, A.; Hoang, A. L.; Tsekouras, G.; Wagner, K.; Lee, C.-Y.; Swiegers, G. F.; Wallace, G. G. A High-Performance Capillary-Fed Electrolysis Cell Promises More Cost-Competitive Renewable Hydrogen. *Nat. Commun.* **2022**, *13* (1), 1304.

(63) Nouri-Khorasani, A.; Tabu Ojong, E.; Smolinka, T.; Wilkinson, D. P. Model of Oxygen Bubbles and Performance Impact in the Porous Transport Layer of PEM Water Electrolysis Cells. *Int. J. Hydrogen Energy* **2017**, *42* (48), 28665–28680.

(64) Lees, E. W.; Mowbray, B. A. W.; Parlane, F. G.; Berlinguette, C. P. Gas Diffusion Electrodes and Membranes for CO_2 Reduction Electrolysers. *Nat. Rev. Mater.* **2021**, 55–64.

(65) Wei, Z. D.; Ji, M. B.; Chen, S. G.; Liu, Y.; Sun, C. X.; Yin, G. Z.; Shen, P. K.; Chan, S. H. Water Electrolysis on Carbon Electrodes Enhanced by Surfactant. *Electrochim. Acta* **2007**, *52* (9), 3323–3329.

(66) Zeng, K.; Zhang, D. Recent Progress in Alkaline Water Electrolysis for Hydrogen Production and Applications. *Prog. Energy Combust. Sci.* **2010**, *36* (3), 307–326.

(67) Bird, R. B.; Stewart, W. E.; Lightfoot, E. N. *Transport Phenomena*, 2nd ed.; Wiley: New York, USA, 2002.

(68) Sforza, P. *Drag Estimation*; 2014.

(69) Gerhardt, M. R.; Pant, L. M.; Bui, J. C. M.; Crothers, A. R.; Ehlinger, V. M.; Fornaciari, J. C.; Liu, J.; Weber, A. Z. Methods—Practices and Pitfalls in Voltage Breakdown Analysis of Electrochemical Energy-Conversion Systems. *J. Electrochem. Soc.* **2021**.

(70) Chen, L.; Oener, S. Z.; Fabrizio, K.; Boettcher, S. W. Design Principles for Water Dissociation Catalysts in High-Performance Bipolar Membranes. *Nat. Commun.* **2022**, *13*, 1–10.

(71) Powers, D.; Mondal, A. N.; Yang, Z.; Wycisk, R.; Kreidler, E.; Pintauro, P. N. Freestanding Bipolar Membranes with an Electrospun Junction for High Current Density Water Splitting. *ACS Appl. Mater. Interfaces* **2022**, *14* (31), 36092–36104.

Table of Contents Graphic

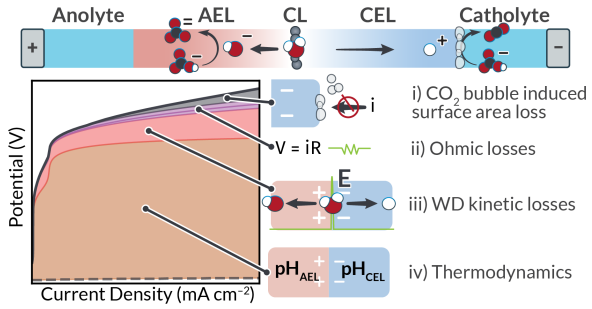

Continuum modeling elucidates non-equilibrium behavior in bipolar membranes (BPMs) employed in BPM electrodialysis (ED) carbon-capture systems. The model resolves the dominant contributions to applied voltage in BPM-ED, identifying CO_2 bubble mitigation and water dissociation as the key areas for improvement in next-generation BPM-ED carbon capture systems.